

37 **Plain Language Summary**

38 Continental China is characterized by Cenozoic active tectonics and intensive earthquakes widely
39 distributed along major fault zones. Therefore, a high-resolution rate model based on the latest
40 GNSS observation is of great importance in explaining such phenomena. This work introduces a
41 novel multiscale spherical spline method that can adapt to discrete data at medium and high
42 latitudes to remove the distortions caused by the conventional method in the Cartesian coordinate
43 system. The rigid-body rotation and spherical harmonic checkerboard detection are utilized to
44 validate the feasibility and resolution of the approach. GNSS data are collected from the most
45 recent studies to estimate the high-resolution strain rate of continental China. Meanwhile, we
46 analyze the correlation between strain rate and focal mechanisms and interpret the deformation
47 and seismicity in continental China.

48 **1 Introduction**

49 Using GNSS velocity data estimating strain rate field has been studied for a long time (Hori
50 et al., 2001; Savage et al., 2001; Shen et al., 2001). Even though the researchers use roughly the
51 same data set, the results are not entirely consistent (Jiang & Liu, 2010; Rui & Stamps, 2019;
52 Wang & Shen, 2020; Wu et al., 2009), which is mainly relative to their method. According to the
53 distinction of using coordinates, estimating strain rate fields using GPS velocity data can be
54 divided into Cartesian and spherical. Delaunay triangulation is always used in the Cartesian
55 coordinate system because Delaunay triangulation in the sphere involves a highly complex
56 algorithm and is time-consuming. This method has the advantage of being less computationally
57 intensive but is error-sensitive and does not guarantee first-order continuity of the strain rate. As a
58 common geostatistical method, Kriging interpolation can also fit strain rates using GNSS data (Zhu
59 & Shi, 2011).

60 Nevertheless, Kriging interpolation does not consider the overall spatial correlation of the
61 estimated values enough. It also requires high-quality data, and GNSS data are susceptible to
62 various environmental factors and cannot meet the requirements. Numerous Cartesian coordinate
63 methods always adopt the first-order Taylor series of the velocity field (Okazaki et al., 2021;
64 Savage et al., 2001), then construct and solve the equations system to obtain strain rate. However,
65 this practice is equivalent to linear interpolation, which decreases detail when GNSS stations are
66 sparse. Therefore, this method suits station-dense areas and large-scale surface deformation
67 analysis. Some Cartesian coordinate methods can accurately fit the velocity values (Xiong et al.,
68 2021), but because GNSS velocity data have large errors, over-fitting may cause distortions in the
69 estimation results. Least-squares collocation and multi-surface function can be implemented in the
70 Cartesian and spherical coordinate systems (Rui & Stamps, 2019; Shen et al., 2015; Wang & Shen,
71 2020; Wu et al., 2009). These two methods also do not guarantee the first-order smoothness of the
72 strain rate. The higher-order continuity of the strain rate is critical for the equation of strain
73 compatibility in the continuum mechanics, limiting the application of these methods. The
74 Spherical wavelet and spherical harmonics are pure spherical coordinate algorithms. Moreover,
75 spherical wavelet and spherical harmonics as pure spherical coordinate methods are like
76 trigonometric functions, which might smooth out much detail of strain rate when GPS or GNSS
77 stations are dense (Su et al., 2016; Wu et al., 2009). These methods will not be able to help analyze
78 small-scale deformation and seismic mechanisms.

79 Continental China is a geologically active region with frequent earthquakes. Many
80 researchers use GNSS velocity data and strain rate to study its continued deformation, active

81 tectonics, and seismic activity. The Qinghai-Tibet Plateau region is one of the most tectonically
82 active regions in the world, and its continuous deformation and its tectonic implications have
83 always been of concern (Chen et al., 2004; Devachandra et al., 2014; Gan et al., 2007; Liang et al.,
84 2013; Wang et al., 2017; Zhang et al., 2004). Due to the Qinghai-Tibetan plateau's implication, its
85 surroundings are seismically active. Shen et al. (2009) and Qi et al. (2011) used GPS velocity data
86 from the Longmen Mountain area to study active tectonics and seismic hazards in this area. Zhao
87 et al. (2018) studied the tectonic influence and seismic mechanism of the 2017 Jiuzhaigou
88 earthquake. (Shen et al., 2001) analyzed the deformation characteristic of the fault system in the
89 western Tibetan Plateau. (Qu et al., 2018) studied the creeping nature of the crust in the Weihe
90 Basin. In addition to the local region, the continuous deformation and seismicity of the Chinese
91 mainland as a whole are also hot spots for researchers (Liu et al., 2007; Rui & Stamps, 2019; Wang
92 et al., 2011; Wang & Shen, 2020; Wei et al., 2014; Xiong et al., 2021; Yu et al., 2019; Zheng et
93 al., 2017). The continental China region straddles the mid and low latitudes. It is in a particular
94 area of the Asia-European plate where active tectonics and seismic hazards are widely distributed.
95 The compression of the Indian plate located at low latitudes also dramatically impacts the mid-
96 latitude and eastern region of continental China. Therefore, it is necessary to develop a high spatial
97 resolution and latitude-adaptation method to further study continental China's strain rate field,
98 seismic activity, and seismic mechanism. The multi-scale spherical spline method can
99 automatically adapt to the inhomogeneous characteristics of the station distribution. Furthermore,
100 it can ensure the smoothness of the strain rate as well as the discontinuous strain rate near the
101 significant active tectonics. At the same time, the spherical spline method can ensure the second-
102 order continuity of the velocity field, which can provide continuous boundary conditions for
103 numerical simulations such as finite elements.

104 Solving an ill-posed equation is necessary to obtain the velocity or strain rate in the meshed
105 grid regardless of the method used. Because of this problem's ill-posed nature, it can have multiple
106 solutions or no solution. Using a smoothing tool can obtain a relatively reasonable solution but
107 also introduces errors (Gan et al., 2007; Ge et al., 2013; Shen et al., 1996; Tape et al., 2009; Wu et
108 al., 2011). Assessing effectiveness and resolution is always a significant issue for solving inverse
109 problems. Scholars studying geophysical inverse problems realized the importance of method
110 uncertainty and resolution in determining the solution (Backus, 1967, 1968, 1970; Franklin, 1970;
111 Wiggins, 1972). Calculating strain rate using GPS or GNSS velocity is a typical ill-posed problem.

112 Many researchers currently use synthetic models to test their methods, but these models all
113 have drawbacks. Some synthetic models can only be adapted to the distribution of stations in a
114 specific study area and tectonic structures (Tape et al., 2009). Other methods are to fit a particular
115 function and judge the merit of the method by the goodness of fit (Tape et al., 2009; Wu et al.,
116 2011). However, the general function shows different values in the specific range, so these tests
117 do not give a resolution of the different areas of the method, and the degree of fit is not easy to
118 observe directly. Many scholars use statistical techniques to determine the accumulation of errors
119 due to smoothings, such as calculating the variance or standard deviation (Jiang et al., 2014;
120 Masson et al., 2014; Tape et al., 2009; Wu et al., 2009; Zhu & Shi, 2011). Nevertheless, the
121 statistical parameters can only represent the overall error situation and do not provide good error
122 discrimination for local areas. Therefore, building a universal set of standards to judge the
123 uncertainty of calculating strain rate by using GNSS velocity data is essential.

124 The Cartesian coordinate methods still use geometric equations based on Cartesian
125 coordinates to calculate strain rates. When researchers estimate the strain rate using Cartesian

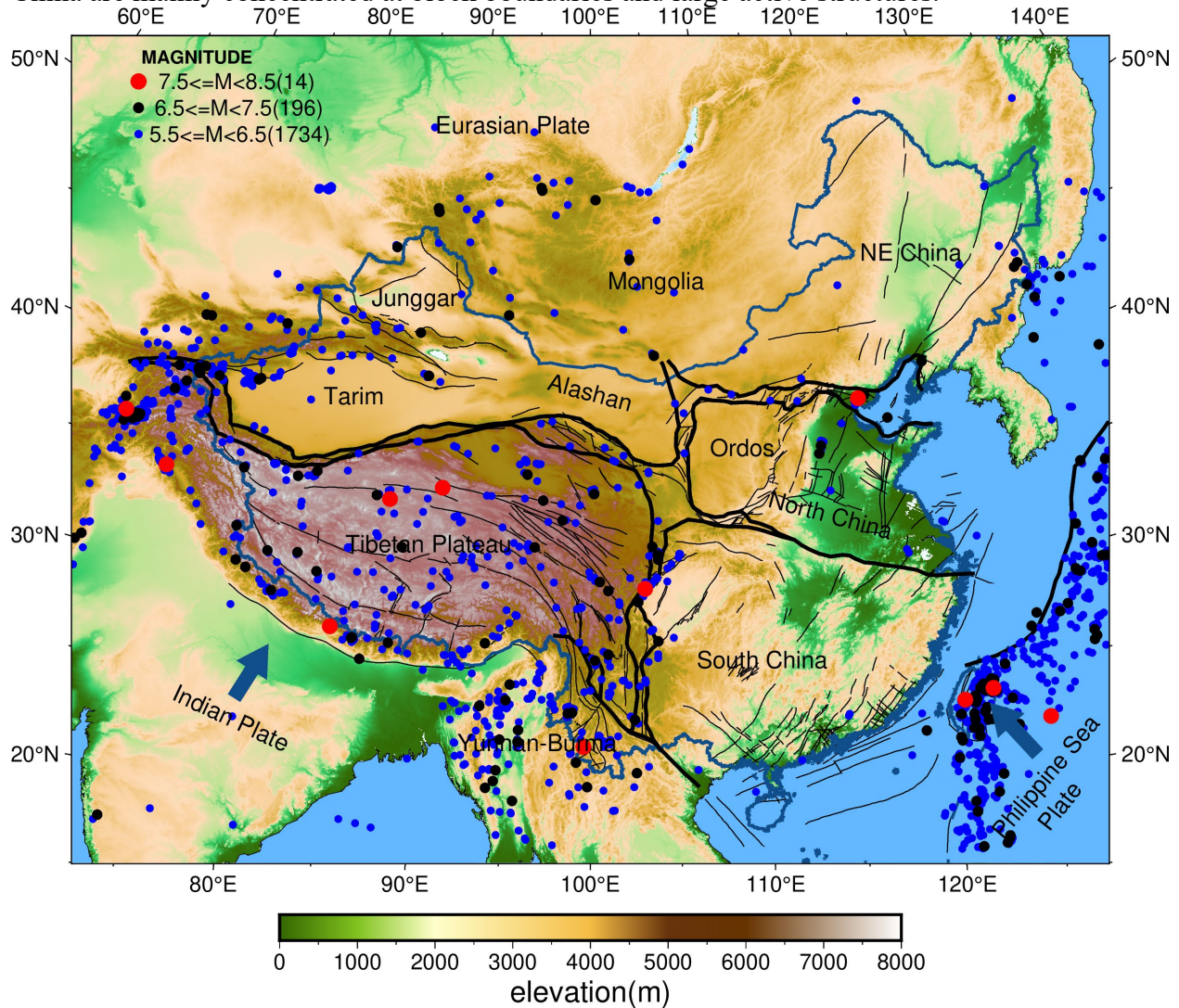
126 geometric equations in the sphere, the error can be ignored in low-latitude areas but can not be
127 neglected in high-latitude study areas. It is also a problem with the Cartesian coordinate methods,
128 so they are suitable for low-latitude areas but not high-latitude areas. In this paper, we use a rigid
129 body rotation model to verify the superiority of the spherical coordinate method. Checkerboard
130 test in seismic tomography is widely appreciated in geophysical inverse problem resolution tests
131 (Day et al., 2001; Glahn et al., 1993; Graeber et al., 2002; Rawlinson et al., 2014; Walck & Clayton,
132 1987). The model consists of a regular grid of alternating positive and negative values, which can
133 also be extended to three dimensions. The advantage of the checkerboard test is that it can detect
134 the resolution and uncertainty of seismic wave inversion results visually and quickly. Because
135 GNSS stations are limited and there are few sampling points in local areas, we imitate the
136 checkerboard test using a spherical harmonic function to check the resolution of the strain rate
137 calculation method. The spherical harmonic function is a continuous function that exhibits a
138 regular lattice of positive and negative values under certain circumstances. We judge the method's
139 merits by observing the degree of recovery of the spherical harmonic function by the inversion
140 method. Using the spherical harmonic test model, we can also conclude that the spherical spline
141 algorithm possesses high resolution.

142 In this article, we first introduce the spherical spline smoothing algorithm and method of
143 calculating strain rate. Then, using the 3571 station sites of continental China and its surroundings
144 from CMONOC I, CMONOC II, and the other sources, we establish a rotation of the rigid body
145 and spherical harmonics models to examine the spherical spline smoothing algorithm. Finally, we
146 calculate the strain rate field in continental China, analyze the correlation between the strain rate
147 field and the earthquake source mechanism, and discuss the earthquake rate in continental China.

148 **2 Seismic Activity and Tectonics Setting of Continental China**

149 The seismic zone in continental China extends along active faults and orogenic zones and
150 is very active (Wang et al., 2001; Yin, 2010). Figure 1 shows recent earthquake events and a
151 significant tectonic setting in mainland China following Li et al. (2012), Xu et al. (2017), Yang et
152 al. (2014), and Zhang (2013). The plate tectonics of continental China is complex. In general, it
153 is divided into two major domains, east and west (i.e., Wang et al., 2011; Zheng et al., 2013), based
154 on $105^{\circ}E$ (i.e., Liu et al., 2007; Rui & Stamps, 2019). Eastern China mainly includes the NCB
155 (Northeast China Block), the NCC (North China Craton), and the SCB (South China Block).
156 Northeast China is part of the Eurasian plate, and the vast Songliao Basin is rich in oil and gas
157 resources. At the same time, the Yilan-Yitong Fault and the Changbai Mountain Range are
158 surrounded by frequent seismic activity. Separated from the Northeast Block by the ZBFZ
159 (Zhangjiakou-Bohai Fault Zone), the NCC consists of the North China Plain, Ordos Block, and
160 the SRZ (Shanxi Rift Zone) (Wang & Shen, 2020; Zheng et al., 2013). Their border zones are all
161 very seismically active areas, and the Tangshan earthquake occurred at the intersection of the
162 ZBFZ and the TLFZ (Tan-Lu Fault Zone). The SCB and the NCC are divided by the Qinling-
163 Dabie Suture Zone. The SCB consists of the Yangzi Craton and the South China Fold Belt
164 separated by the Jiao-Shao Fault (Zheng et al., 2013). This area is relatively stable and with few
165 major earthquakes. Western China consists mainly of the Qinghai-Tibet Plateau and several
166 important basins and blocks (i.e., Tarim, Qaidam, Junggar, and Alashan), which are divided by
167 several large faults and orogen belts (i.e., West and East Kunlun Fault, ATF (Altyr Tagh Fault),
168 Qilian-Haiyuan Fault, and South and North Tian Shan Orogen belt). Because the Qinghai-Tibet
169 Plateau is directly extruded by the northeastern direction of the Indian Plate, its interior and the
170 Himalayan Orogenic Belt at the boundary are highly seismic.

171 Moreover, the extrusion of the Qinghai-Tibet Plateau to the east collided with the South
 172 China block, causing frequent earthquakes in the Xianshuihe-Xiaojiang Fault and the Longmen
 173 Shan Fault, which are ones of the world's most active faults and where the Wenchuan earthquake
 174 occurred. The North and South Tianshan, orogenic belts above the northern part of the Tibetan
 175 Plateau, are also very involved in seismic activity because of the far-field effect of the Indian plate
 176 thrusting (Yin & Harrison, 2000). Seismicity in the eastern region is weaker than in the western
 177 part of China in terms of magnitude and frequency, and earthquakes in both western and eastern
 178 China are mainly concentrated at block boundaries and large active structures.



179
 180 **Figure 1.** A simple tectonic unit and distribution of earthquake in continental China. The black
 181 lines are boundaries of blocks; the deep arrows donate the subduction direction of the Pacific plate

182 and the Indian Ocean plate; the color dots show seismic hazards with $M \geq 5.5$ from January 1,
183 1960, to December 31, 2021.

184 3 Spherical Spline Method

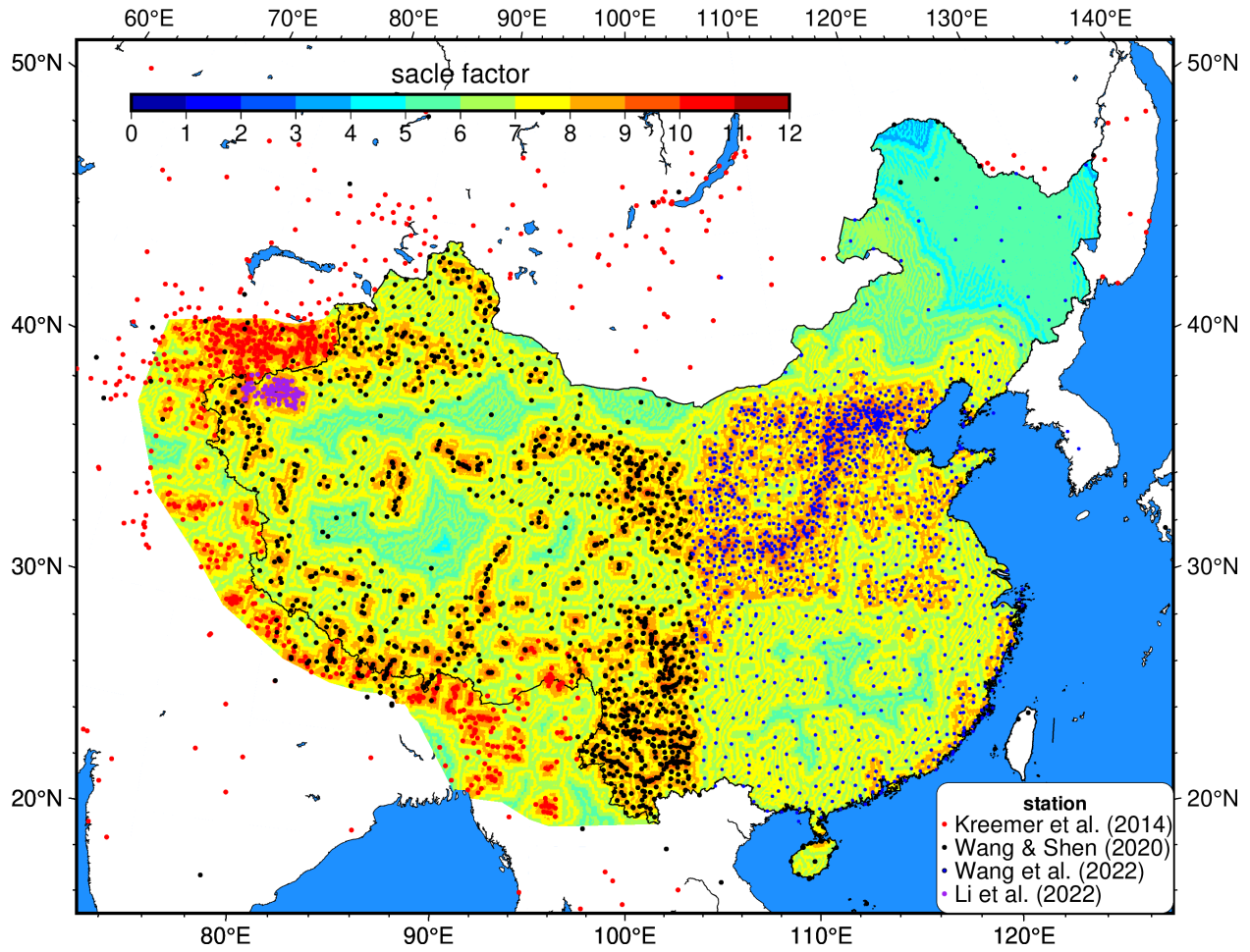
185 3.1 Gird Meshing and Choosing Scale Factor

186 Gird meshing in a sphere is always the research focus and previous steps of the
187 interpolation algorithm of discrete data in the spherical surface. This study adopts the method of
188 making spherical surface mesh high-resolution grids with spherical equilateral triangular (Wang
189 & Dahlen, 1995; Wang et al., 1998), which has been used in many studies (Hao et al., 2019; Su et
190 al., 2016; Tape et al., 2009). It is acknowledged that a spherical surface can not be arbitrarily
191 divided into equilateral triangular being like a plane because a maximum of twenty spherical
192 equilateral triangular can be divided on a spherical surface. We link the midpoints of an equilateral
193 triangle to each other, which makes us obtain four equilateral triangles. Then, by repeating this
194 operation, we can get high-resolution grids. We also link the trisection point, which can make us
195 bring mesh of any density cooperating connecting the midpoint. We make a list of relationships
196 with scale factor q (numbers of repeating), numbers of grids (Faces), and spatial support (average
197 angular distance ($\bar{\Delta}$) and side arclength (l)).

198 **Table 1.** The relationship between scale factor and spatial scale.

q	Scale		Spatial support	
	Faces	$\bar{\Delta}$	l	
0	20	63.435°	7053.64km	
1	80	31.718°	3526.82km	
2	320	15.859°	1763.41km	
3	1280	7.929°	881.71.km	
4	5120	3.965°	440.85km	
5	20480	1.982°	220.43km	
6	81920	0.991°	110.21km	
7	327680	0.496°	55.11km	
8	1310720	0.248°	27.55km	
9	5242880	0.124°	13.78km	
10	20971520	0.062°	6.78km	
11	83886080	0.031°	3.44km	
12	335544320	0.016°	1.72km	

199 We must choose a scale factor for ourselves using the spherical spline algorithm. In this
200 study, we only discuss the scale factor of the station in mainland China and its surrounding regions,
201 and Figure 2 shows the situation of grids meshing for $q=12$. We have observed that areas with
202 $q=9,10$ are small, and $q=11,12$ is none. Finally, we chose $q=10$ meshing grids in our study. For
203 other situations, the scale factor is selected from 7 to 9 and is not more than 12 (Tape et al., 2009).



204

205 **Figure 2.** Station of mainland China and example of meshing scale using $q=0-12$. All station
 206 locations are from Wang & Shen (2020), Wang et al. (2022), and Li et al. (2022). The red dots
 207 denote GPS stations around continental China combined by Kreemer et al. (2014), which have
 208 been used by Wang & Shen (2020) in their research; The black dots represent the GPS station from
 209 Wang & Shen (2020); The deep blue dots represent the GPS station from Wang et al. (2022); The
 210 purple dots represent the GPS station from Li et al. (2022). Where stations are dense, the meshing
 211 of continental China with $q=5-12$ is available.

212

3.2 Basis Function of Spherical Spline

213

214

We utilize the GNSS station site to define the basic function of the spherical spline
 (Lancaster & Salakauskas, 1986).

$$f = \begin{cases} \frac{3}{4}\bar{\Delta}^{-3}\Delta^3 - \frac{6}{4}\bar{\Delta}^{-2}\Delta^2 + 1, & \Delta \leq \bar{\Delta}, \\ -\frac{1}{4}\bar{\Delta}_1^3 + \frac{3}{4}\bar{\Delta}_1^2 - \frac{3}{4}\bar{\Delta}_1 + \frac{1}{4}, & \bar{\Delta} \leq \Delta \leq 2\bar{\Delta} \end{cases} \quad (1)$$

216

217

where Δ is the angular distance between grid nodes with the station site, $\bar{\Delta} = \frac{\arccos\left(\frac{\cos(72^\circ)}{1-\cos(72^\circ)}\right)}{2^q}$ is the
 angular distance of adjacent grid nodes and $\bar{\Delta}_1 = \frac{\bar{\Delta}-\Delta}{\bar{\Delta}}$. We define θ, φ as codimension and

218 longitude of station sites and θ', φ' as codimension and longitude of grid nodes. According to
 219 spherical trigonometry, $\Delta = \text{acos}[\cos \theta' \cos \theta + \sin \theta' \sin \theta \cos(\varphi' - \varphi)]$.

220 Function (2) and function (3) show the basic function of the spherical spline of the first
 221 derivative,

$$222 \quad \begin{cases} \frac{\partial f}{\partial \theta} = \frac{1}{\bar{\Delta}} \left(\frac{9}{4} \bar{\Delta}^{-2} \Delta^2 - 3\bar{\Delta}\Delta \right) \frac{\partial \Delta}{\partial \theta} \\ \frac{\partial f}{\partial \varphi} = \frac{1}{\bar{\Delta}} \left(\frac{9}{4} \bar{\Delta}^{-2} \Delta^2 - 3\bar{\Delta}\Delta \right) \frac{\partial \Delta}{\partial \varphi} \end{cases} \quad 0 \leq \Delta \leq \bar{\Delta}, \quad (2)$$

$$223 \quad \begin{cases} \frac{\partial f}{\partial \theta} = \frac{1}{\bar{\Delta}} \left(-\frac{3}{4} \bar{\Delta}_1^2 + \frac{3}{2} \bar{\Delta}_1 - \frac{3}{4} \right) \frac{\partial \Delta}{\partial \theta} \\ \frac{\partial f}{\partial \varphi} = \frac{1}{\bar{\Delta}} \left(-\frac{3}{4} \bar{\Delta}_1^2 + \frac{3}{2} \bar{\Delta}_1 - \frac{3}{4} \right) \frac{\partial \Delta}{\partial \varphi} \end{cases} \quad \bar{\Delta} \leq \Delta \leq 2\bar{\Delta}. \quad (3)$$

224 When station sites and grid nodes are superposition ($\Delta = 0$), we use function (4) as the
 225 basic function.

$$226 \quad f = 1 \quad \frac{\partial f}{\partial \varphi} = 0 \quad \frac{\partial f}{\partial \theta} = 0 \quad (4)$$

227 And when Δ is more than $2\bar{\Delta}$, we use function (5) as the basic function.

$$228 \quad f = 0 \quad \frac{\partial f}{\partial \varphi} = 0 \quad \frac{\partial f}{\partial \theta} = 0 \quad (5)$$

229 3.3 Decomposition of the Velocity Field in Spherical Spline

230 The velocity field tangent to the sphere can be resolved as the sum of two vectors (function
 231 (6)),

$$232 \quad v(\theta, \varphi) = v_\lambda(\theta, \varphi) \hat{\theta} + v_\varphi(\theta, \varphi) \hat{\varphi}, \quad (6)$$

233 where $\hat{\theta}$, $\hat{\varphi}$ are two unit vectors with south-north and east-west directions and θ, φ is
 234 codimension and longitudes of station sites. It is acknowledged that any scalar function $g \in$
 235 $L^2(S^2)$ can be written as the product of two vectors,

$$236 \quad g(x, y) = \sum_{k=1}^M m_k g_k(x, y) = g_k^T(x, y) m. \quad (7)$$

237 Thus, function (6) can be rewritten as

$$238 \quad v(\theta, \varphi) = \sum_{k=1}^M a_k f_k(\theta, \varphi) \hat{\theta} + \sum_{k=1}^M b_k f_k(\theta, \varphi) \hat{\varphi}. \quad (8)$$

239 Function (8) is discrete by observation sites (θ_i, φ_i) , $i = 1, \dots, N$, as

$$\begin{cases} v_{\theta}^i = \sum_{k=1}^M a_k f_k(\theta_i, \varphi_i) + n_{\theta}^i \\ v_{\varphi}^i = \sum_{k=1}^M b_k f_k(\theta_i, \varphi_i) + n_{\varphi}^i \end{cases}, \quad (9)$$

where $v_{\theta}^i, v_{\varphi}^i$ are the velocity of the solo station whose observation errors are denoted by $n_{\theta}^i, n_{\varphi}^i$. Two equations of function (9) possess the same form; thus, estimation methods of a_k, b_k are also the same. We rewrite function (9) as matrix form,

$$\mathbf{d} = \mathbf{Fm} + \mathbf{n}, \quad (10)$$

where \mathbf{d} is a column vector composed by v_{θ}^i or v_{φ}^i , \mathbf{F} is a designed matrix composed of a quantity of spherical spline basis function, \mathbf{m} is a column vector consisting of the model parameter, which is an unknown quantity to be solved, and \mathbf{n} is a column vector composed of observation error. Function (10) is an ill-posed equation whose solution is not unique. Thus, we obtain model parameter \mathbf{n} by least-squares functional,

$$G(\mathbf{m}) = \frac{1}{2}(\mathbf{Fm} - \mathbf{d})^T \mathbf{C}_D^{-1}(\mathbf{Fm} - \mathbf{d}) + \frac{1}{2}\lambda^2 \mathbf{m}^T \mathbf{S} \mathbf{m}, \quad (11)$$

where λ controls the smoothness of the solution. Then we make $\frac{dG(\mathbf{m})}{d\mathbf{m}} = 0$ and get

$$\mathbf{m} = (\mathbf{F}^T \mathbf{C}_D^{-1} \mathbf{F} + \lambda^2 \mathbf{S})^{-1} \mathbf{F}^T \mathbf{C}_D^{-1} \mathbf{d}, \quad (12)$$

where \mathbf{C}_D is east and north velocity correlation acquired on GPS velocity data files. Moreover, we select λ by ordinary cross-validation (Tape et al., 2009). In this section, we only introduce the fitting of the velocity field, but calculating the velocity gradient method is the same.

3.4 Calculating the Strian Field

Calculating the strain rate in our study looks like a three-dimensional spherical surface. Still, we do not obtain radial derivate of velocity component due to GPS or GNSS station observing only above the earth's surface. So, we do not discuss the radial strain rate on the spherical surface. Then it is related to v_{φ}, v_{θ} when calculating strain rate from the velocity field. The horizontal strain rate is the divergence and its transpose of GNSS velocities in the spherical coordinate system as

$$\begin{cases} \dot{\varepsilon}_{\theta} = \frac{1}{r} \frac{\partial v_{\theta}}{\partial \theta} \\ \dot{\varepsilon}_{\varphi} = \frac{1}{r \sin \theta} \frac{\partial v_{\varphi}}{\partial \varphi} + \frac{v_{\theta}}{r} \cot \theta \\ 2\dot{\varepsilon}_{\theta\varphi} = \frac{1}{r \sin \theta} \frac{\partial v_{\theta}}{\partial \varphi} - \frac{v_{\varphi}}{r} \cot \theta + \frac{1}{r} \frac{\partial v_{\varphi}}{\partial \theta} \\ 2\dot{\omega}_r = \frac{1}{r} \frac{\partial v_{\varphi}}{\partial \theta} + \frac{v_{\varphi}}{r} \cot \theta - \frac{1}{r \sin \theta} \frac{\partial v_{\theta}}{\partial \varphi} \end{cases}. \quad (13)$$

4 Detection Model

Because of the uneven distribution of stations, it is a significant issue how researchers estimate horizontal strain rates from these stations. Many adopt different methods to integrate and

266 fit the velocity and strain rate fields, but they always obtain different results, even using the same
 267 data sets. Thus, judging a method's merits is a crucial assignment.

268 First, we present a rigid rotation model to illustrate that the spherical coordinate method is
 269 more suitable for calculations on the sphere. Generally, when calculating in the low latitude study
 270 area and small study area, the Cartesian method's result is almost identical to the spherical
 271 coordinate method. However, the Cartesian coordinate method cannot undertake this mission when
 272 the studied area is large-wide or high-latitude.

273 In addition, we present a spherical harmonics model. We use the spherical spline method
 274 to fit the spherical harmonic values generated by the latitude and longitude of each station and
 275 compare the results with the theoretical spherical harmonic values to determine the precision and
 276 resolution by analogy with the checkerboard test of seismic tomography (Bürgmann, 2005; Lanza
 277 et al., 2020; Loveless & Meade, 2010; Métois et al., 2012). It can help us visually judge the merits
 278 and effectiveness of the method in study areas.

279 4.1 Rigid Body Rotation

280 We assume continental China and its surrounding areas are located inside a rigid plate that
 281 only orbits a synthetic Euler polar with an angular velocity of $5 \times 10^{-8} \text{ rad/yr}$. Then we
 282 calculate the linear velocity component v_θ (south-north direction), v_φ (east-west direction) of
 283 every station in our study areas. When a plate as a rigid body revolves, it has no deformation. The
 284 normal and shear strain rates are zero relative to the angular velocity. The rotation rate is not zero.

285 Function (14) is the relationship between v_θ, v_φ with latitude and longitude of the Euler
 286 polar.

$$287 \begin{cases} v_\theta = R\Omega \sin(\varphi - \varphi') \sin \theta' \\ v_\varphi = R\Omega [\cos \varphi \cos \varphi' \cos \theta \cos \theta' - \cos \theta' \sin \theta + \cos \theta \sin \varphi \sin \varphi' \sin \theta'] \end{cases} \quad (14)$$

288 According to functions (13-14), we have the rotation rate

$$289 \omega_{\theta\varphi} = -\frac{\Omega}{\sin \theta} (\sin \varphi \sin \varphi' \sin \theta' + \cos \varphi \cos \varphi' \sin \theta' + \cos \theta \cos \theta' \sin \theta$$

$$290 \quad - \cos \varphi \cos \varphi' \cos^2 \theta \sin \theta' - \cos^2 \theta \sin \varphi \sin \varphi' \sin \theta'),$$

291 (15)

292 where θ, φ denote codimension and latitude of GPS or GNSS stations, θ', φ' denote codimension
 293 and latitude of the polar axis, R is the radius of the earth, 6371 km and Ω is angular velocity.
 294 Meanwhile, we also get a normal strain rate, and the shear strain rate is zero, which can illustrate
 295 that function (14) is correct. Then we input the velocity of stations into a spherical spline program
 296 to obtain fitting velocity and rotation rate compared with the theoretical results of the entire study
 297 area.

298 4.2 Spherical Harmonics

299 The spherical harmonics function is widely applied in the spherical coordinate system. In
 300 geophysical studies, we often take the earth as a research object. Because the earth's shape is
 301 approximately a sphere, its physics field possesses a spherical symmetric future. Thus, spherical
 302 harmonics are widely used in geodesy, meteorology, spherical finite element, and numerical
 303 simulation of geodynamics.

304 We use function (16) to build our spherical harmonics model,

$$305 \quad Y_l^m(\theta, \varphi) = \sqrt{\frac{(2l+1)(l-m)!}{4\pi(l+m)!}} P_l^m(\cos\theta)e^{im\varphi}, \quad -l \leq m \leq l, \quad (16)$$

306 where l, m are the order and degree of spherical harmonics, i is the imaginary unit and $P_l^m(x)$ is
 307 Associated Legendre Polynomial and,

$$308 \quad P_l^m(x) = (-1)^m(1-x^2)^{\frac{m}{2}} \frac{d^m}{dx^m}(P_l(x)).$$

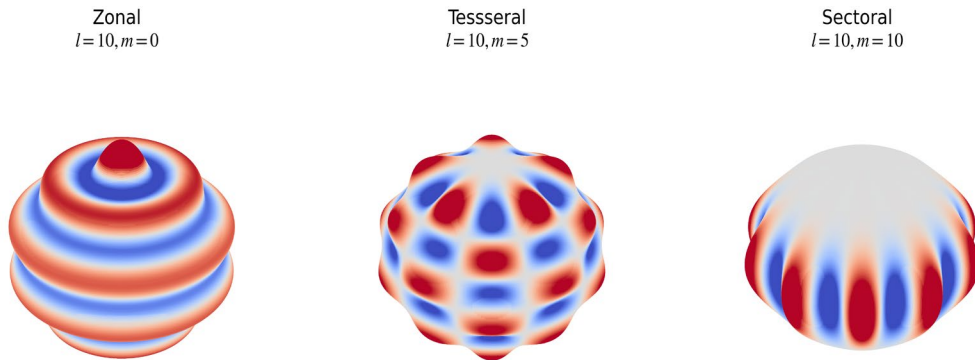
309 $P_l(x)$ is Orthogonal Legendre polynomial,

$$310 \quad P_l(x) = \frac{1}{2^l l!} \frac{d^l}{dx^l}(x^2-1)^l. \quad (17)$$

311 Due to the feature of spherical harmonics, its distribution takes on transversal, longitudinal
 312 strips or spherical rectangles (Figure 3) when l, m take different numbers. We use the latitude and
 313 longitude of GNSS station sites to calculate spherical harmonics values ($Y_l^m(\theta, \varphi)$) of their site.
 314 Then, v_φ denote the real part of the values and v_θ denote the imaginary part of the values, which
 315 will be inputted into the spherical spline program to obtain fitting velocity and velocity gradient
 316 results. Meanwhile, to show the resolution of the method intuitively, we can calculate the
 317 longitudinal and latitudinal half-wavelength of spherical harmonics with l, m selected by us.
 318 Function (18) is the equation of calculating half-wavelength (Wieczorek & Meschede, 2018),

$$319 \quad \begin{cases} \lambda_l = \frac{2\pi R}{\sqrt{l(l+1)}} \\ \lambda_m = \frac{2\pi R \cos \theta}{l} \end{cases}, \quad (18)$$

320 where λ_l, λ_m are meridional and zonal half-wavelength, θ is colatitude and R is the earth's radius,
 321 6371km.



322

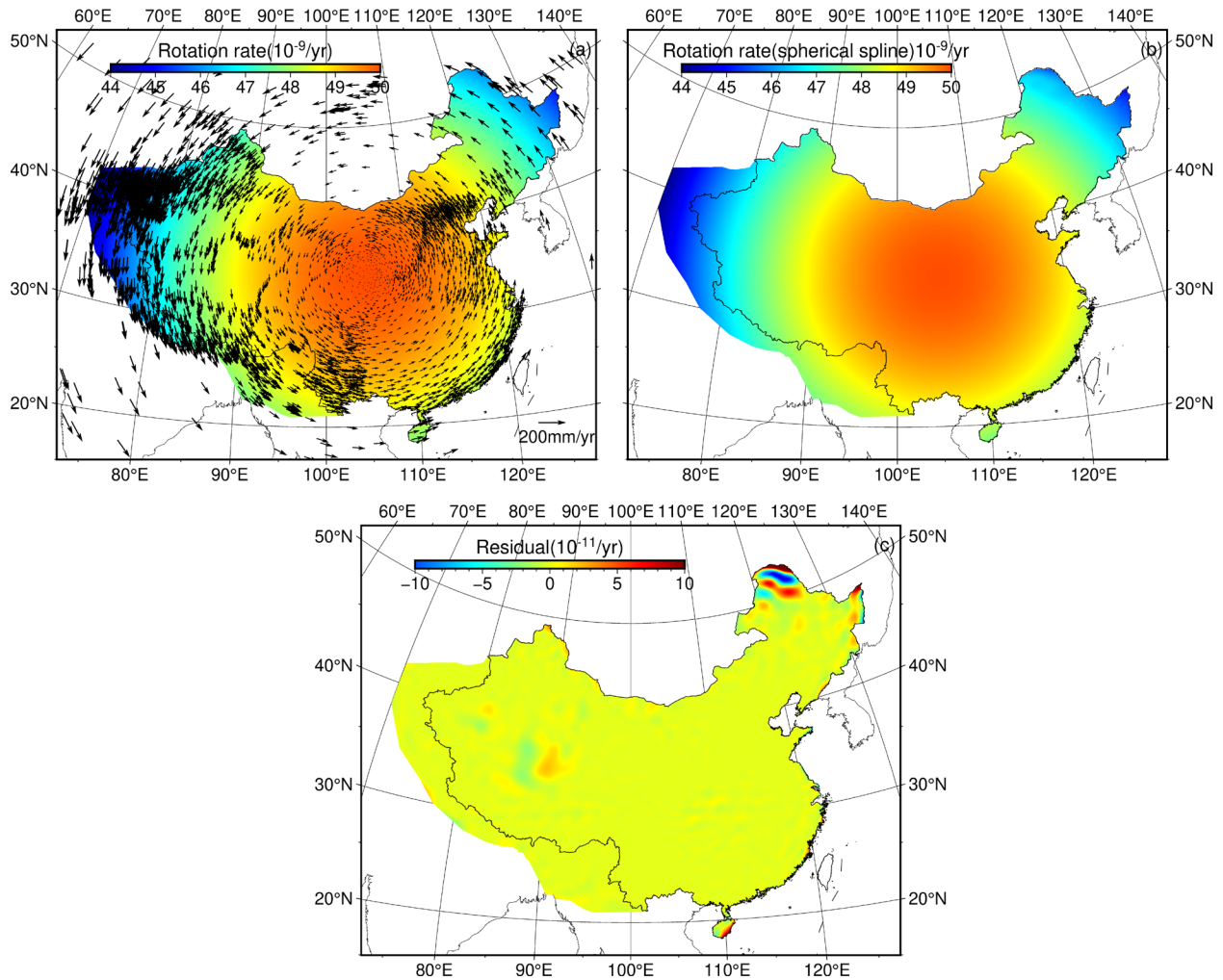
323 **Figure 3.** The shape of the strips or lattices produced by the spherical harmonic function on the
 324 sphere.

325 5 Data and Results

326 In Sections 5 and 6, the stations used by us are from three recent studies (Li et al., 2022;
327 Wang & Shen, 2020; Wang et al., 2022). Wang & Shen (2020) supply complete GPS velocity data
328 for continental China and its surroundings and this dataset has been adopted in many studies (Ge
329 et al., 2022; Li et al., 2021; Pang et al., 2023; She & Fu, 2020; Wang et al., 2022; Zhu et al., 2022).
330 The data set combines the CMONOC I, CMONOC II, and some regional densified stations in
331 continental China, and their observations span from 1991 to 2016. In addition, he has assembled
332 data from several other studies to compensate for the lack of data from surrounding continental
333 China (Kreemer et al., 2014). We then use the North China dataset from Wang et al. (2022) to
334 densify data in Ordos Block and replace the overlapping station portion between this dataset and
335 the dataset from Wang & Shen (2020). The dataset used by Wang et al. (2022) came from Hao et
336 al. (2021), and it multiplied the uncertainty by 3 to make the data fit the noise of the dataset from
337 Wang & Shen (2020), to be able to use the two sets of data together. Finally, we processed the data
338 set from (2022) using the method of Wang et al. (2022) to densify data in North and South
339 TianShan and replace its overlapping parts between Li et al. (2022) and Wang & Shen (2020).
340 Therefore, we finally assembled the data from 3715 stations in and around continental China and
341 removed 144 groups of stations in which the relative error of one of the velocity components
342 exceeded ten percent and the error of the velocity vector magnitude exceeded thirty percent. The
343 3571 stations we used are labeled in Figure 2.

344 5.1 Inspection Result of Rigid Body Rotation

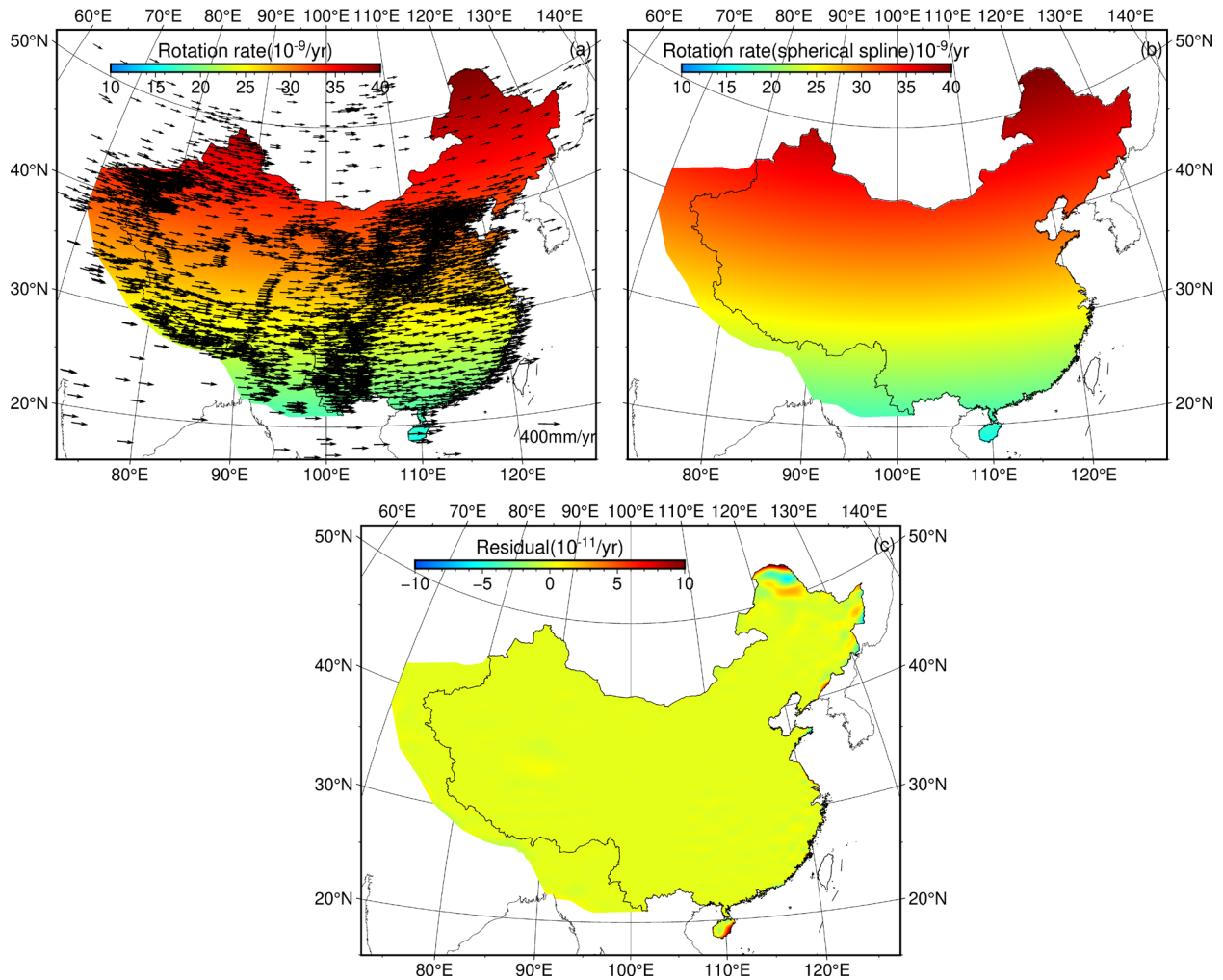
345 Figure 4a shows the artificial linear velocity field (black arrow) of stations revolving
346 around the Euler polar ($90^{\circ}N, 105^{\circ}E$) and theoretical rotation rate (background) correlation with
347 an angular velocity of $5 \times 10^{-8} rad/yr$. Figure 4b shows that the rotation rate calculated by using
348 the spherical spline method is almost identical to the theoretical rotation rate; Figure 4c shows the
349 absolute error of the theoretical and fitting rotation rates. We can observe that the relative error is
350 not more than two thousandths where the difference is largest. In contrast, relative errors in the
351 interior of continental China are mainly under one ten-thousandth. Other strain rate components
352 are calculated by the spherical spline method shown in Figure S1, and their theoretical value is
353 zero. The order of magnitude of the rotation rate is 10^{-8} . Whereas the order of magnitude of strain
354 rate components in Figure S1 is 10^{-11} , and the largest errors are on the boundary. Thus, the result
355 calculated by the spherical spline method can be better.



356

357 **Figure 4.** Theoretical result and estimated result of rotation rate. (a) Theoretical result of rotation
 358 rate and artificial velocity (black arrow). (b) result of the spherical spline. (c) absolute error
 359 (difference between theoretical results and estimated results).

360 Figure 5a shows the linear velocity field (black arrow) of stations revolving around the
 361 Euler polar (35°N, 105°E) and theoretical rotation rate (background) with an angular velocity of
 362 $5 \times 10^{-8} \text{ rad/yr}$; Figure 5b shows that the rotation rate calculated using the spherical spline
 363 method is almost identical to the theoretical rotation rate; Figure 5c shows the absolute error of the
 364 theoretical and fitting rotation rate. The result showed similar characteristics to Figure 4. Other
 365 strain rate components with zero theoretical results are shown in Figure S2, which also indicates
 366 similar futures to Figure S1.



367

368 **Figure 5.** Theoretical result and estimated result of rotation rate. (a) Theoretical result of rotation
 369 rate and synthetic velocity (black arrow). (b) result of the spherical spline. (c) absolute error
 370 (difference between theoretical results and estimated results).

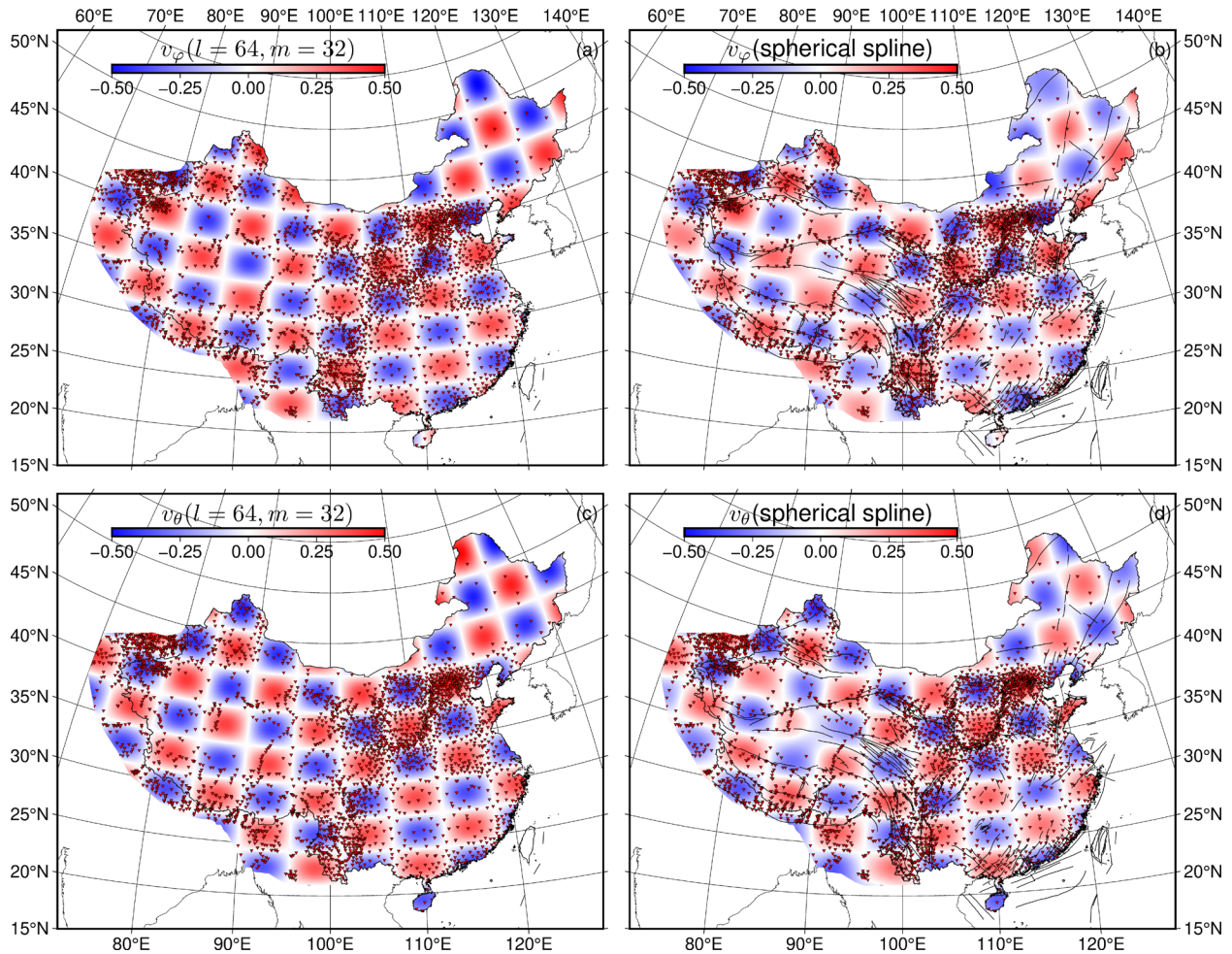
371

5.2 Inspection Result of Spherical Harmonics

372

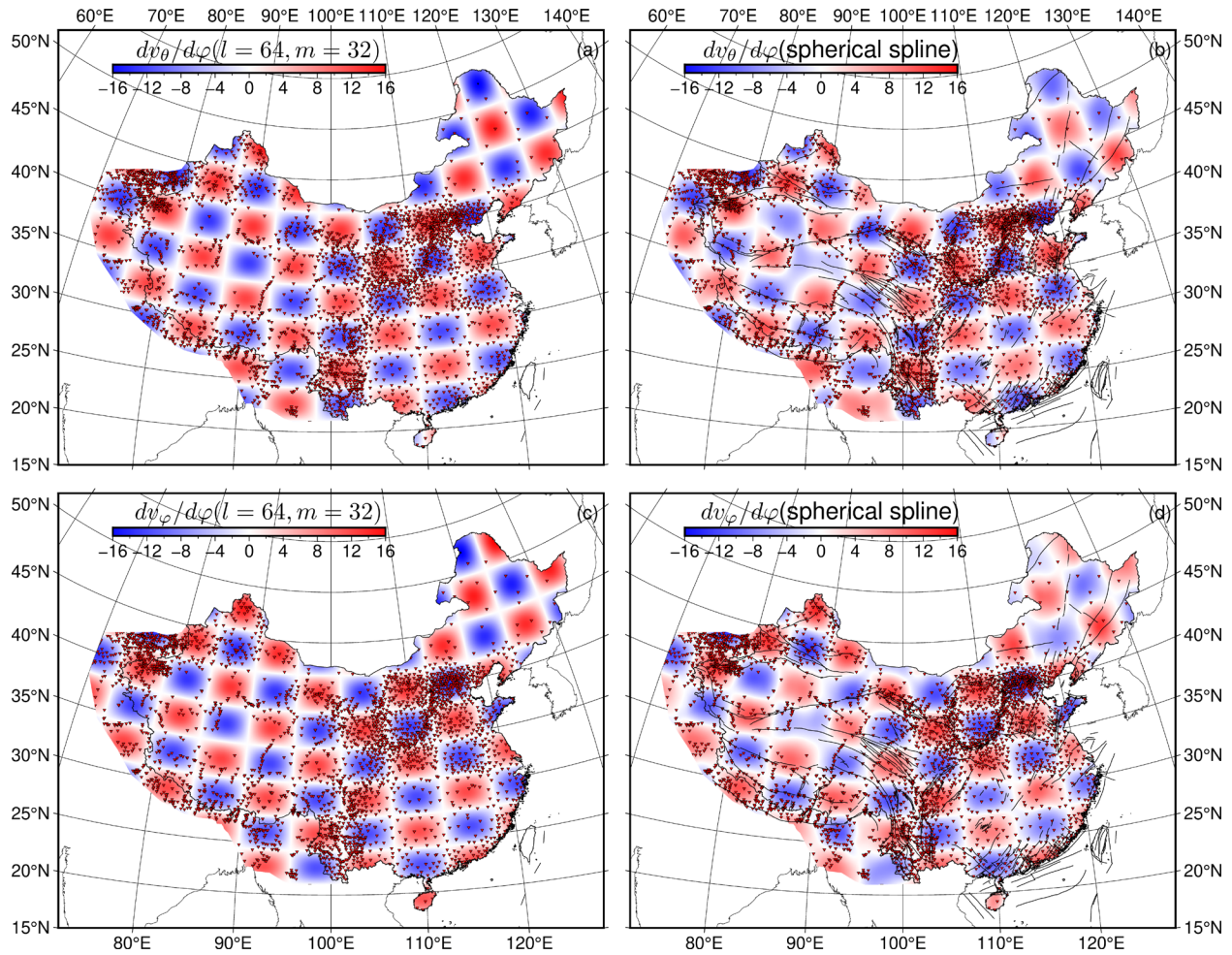
Figure 6 shows the detection result of velocity. Figure 6a and 6c, respectively, show
 373 synthetic gridding v_θ and v_φ , which are imaginary parts and real parts of spherical harmonics with
 374 $l = 64, m = 32$. According to function (22), we can obtain that south-north direction half-
 375 wavelength λ_l is about 620km, earth-west direction half-wavelength λ_m is about 567km at 25°N
 376 and earth-west direction half-wavelength λ_m is about 402km at 50°N. Figure 5b and 6d,
 377 respectively. They exhibit a relationship between the fitting result of spherical spline and station
 378 density. We can observe that where stations are density and uniform, fitting results by spherical

379 spline and theoretical v_θ, v_ϕ are consistent, and where there are no stations (32°N to 37°N, 81°E
 380 to 92°E), the grids of spherical harmonics are blurred, but the shape is still visible.



381
 382 **Figure 6.** The spherical harmonics with $l = 64, m = 32$ and fitting results of the spherical spline.
 383 (a) v_ϕ calculated by spherical harmonics. (b) v_ϕ fitted by spherical spline. (c) v_θ calculated by
 384 spherical harmonics. (d) v_θ fitted by spherical spline. The red inverted triangles are all stations of
 385 continental China and the surroundings from Figure 1, and the black lines on the background
 386 donate significant activity tectonics of continental China (same as Figure 6-9 and Figure S3-S8).

387 Figure 7 shows the detection result of the velocity gradient. Figure 7a and 7c, respectively.
 388 They illustrate synthetic gridding $\frac{dv_\phi}{d\theta}, \frac{dv_\theta}{d\theta}$, which are south-north derivatives of the imaginary part
 389 and the real part of spherical harmonics with $l = 64, m = 32$. The result showed similar
 390 characteristics where stations are density and uniform, fitting the result by spherical spline and
 391 theoretical $\frac{dv_\phi}{d\theta}, \frac{dv_\theta}{d\theta}$ are consistent, and where there are no stations (32°N to 37°N, 81°E to 92°E),
 392 the grids of spherical harmonics are blurred, but the shape is still visible in Figure 7.

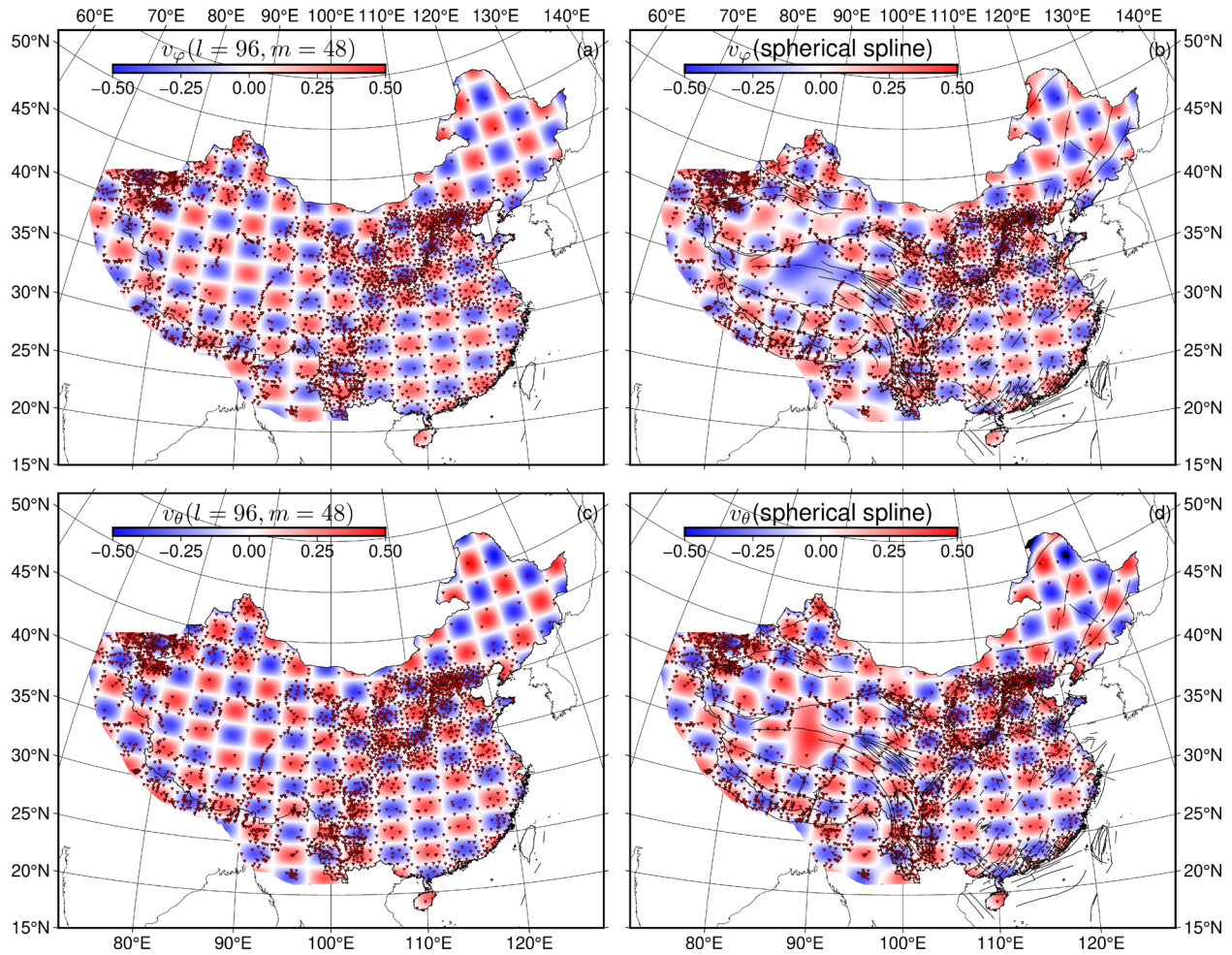


393

394 **Figure 7.** The latitude direction gradient of spherical harmonics with $l = 64, m = 32$ and fitting
 395 results of the spherical spline. (a) $\frac{dv_\varphi}{d\varphi}$ calculated by spherical harmonics. (b) $\frac{dv_\varphi}{d\varphi}$ fitted by spherical
 396 spline. (c) $\frac{dv_\theta}{d\theta}$ calculated by spherical harmonics. (d) $\frac{dv_\theta}{d\theta}$ fitted by spherical spline.

397

398 Figure 8 shows the detection result of velocity using spherical harmonics with $l = 96, m =$
 399 48 to test minimum resolution because its south-north direction half-wavelength λ_l is about
 400 400km , earth-west direction half-wavelength λ_m is about 360km at 25°N and earth-west
 401 direction half-wavelength λ_m is about 260km at 50°N . So, the purpose of this detection model is
 402 to confirm whether the spherical spline method processes the ability to distinguish the strain rate
 403 of minor structures (scale of about 300km) in dense station areas such as the Pamir Plateau,
 404 Tianshan structure zone, Sichuan, Yunnan, Ordos block, North China seismic zone, and South
 405 China region. Figure 8a and 8c, respectively, show artificial gridding v_θ, v_φ , which are imaginary
 406 parts and real parts of spherical harmonics with $l = 96, m = 48$. Figure 8b and 8d, respectively.
 They show the relationship between the fitting result of spherical spline and station density.

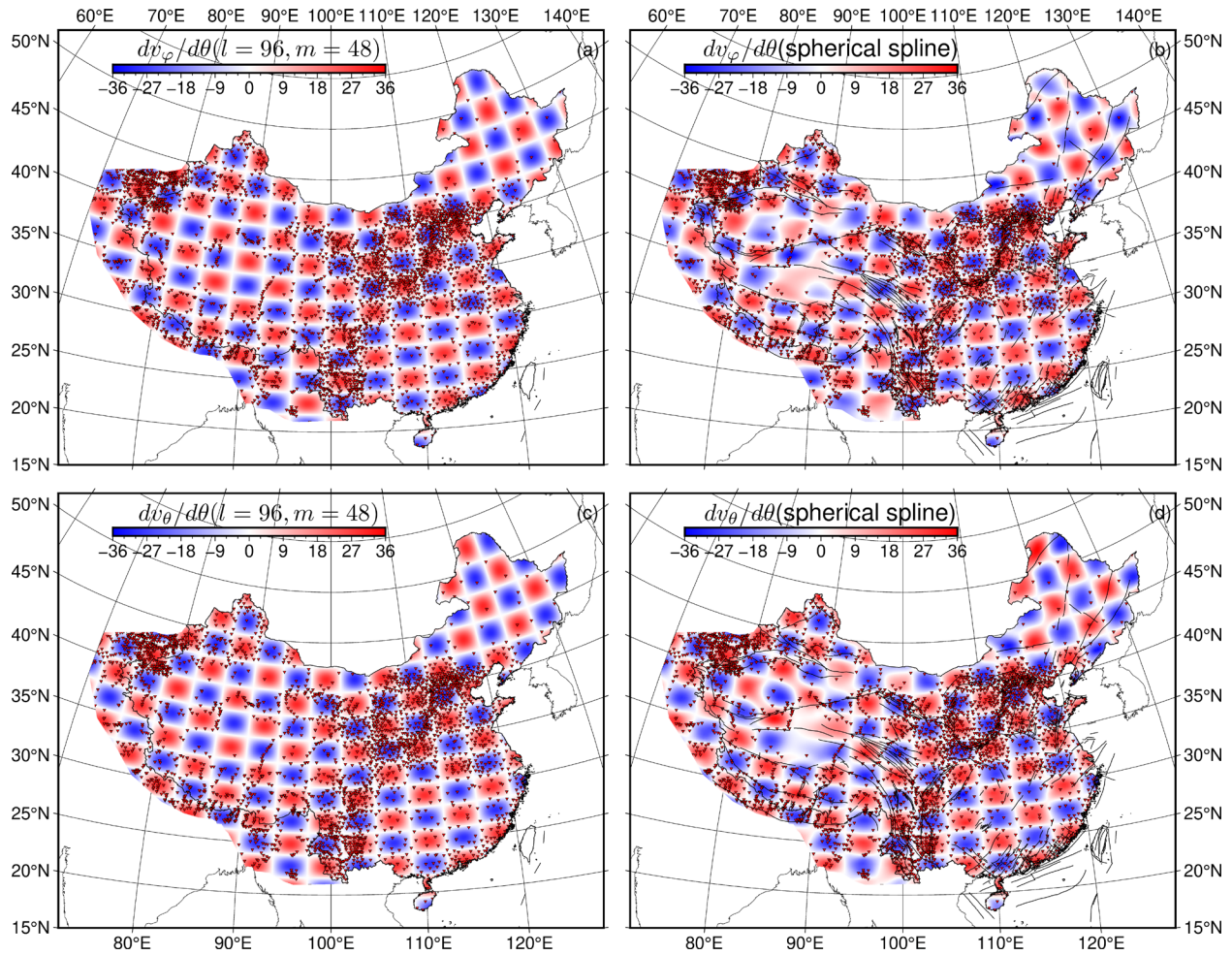


407

408 **Figure 8.** Spherical harmonics with $l = 98, m = 64$ and fitting results of the spherical spline. (a)
 409 v_φ calculated by the spherical harmonics function. (b) v_φ fitted by spherical spline. (c) v_θ
 410 calculated by spherical harmonics function; (b) v_θ fitted by spherical spline.

411 Figure 9 shows the fitting detection result of velocity. Figure 9a and 9c, respectively. They
 412 show synthetic gridding $\frac{dv_\varphi}{d\theta}, \frac{dv_\theta}{d\theta}$, which are south-north derivatives of the imaginary part and real
 413 part of spherical harmonics with $l = 96, m = 48$. The result showed similar characteristics where
 414 stations are density and uniform. Fitting the result by spherical spline and theoretical $\frac{dv_\varphi}{d\theta}, \frac{dv_\theta}{d\theta}$ are
 415 consistent with figure 9. The results of all strain rates are the sum of the multiples of velocity and
 416 velocity gradient. Their characteristics are like the above results. So, they are not shown in the
 417 main text but in Figure S3-S8.

418 From the results of the above two experiments, we can conclude that the spherical spline
 419 results we can still give confidence to the strain rate results calculated by the spherical spline of
 420 large structures over 600 km in areas where stations are sparse or even absent. Furthermore, in
 421 areas with dense or uniform stations, the spherical spline can also reveal the correspondence
 422 between structures and strain rates at scales below 300 km or even smaller.



423

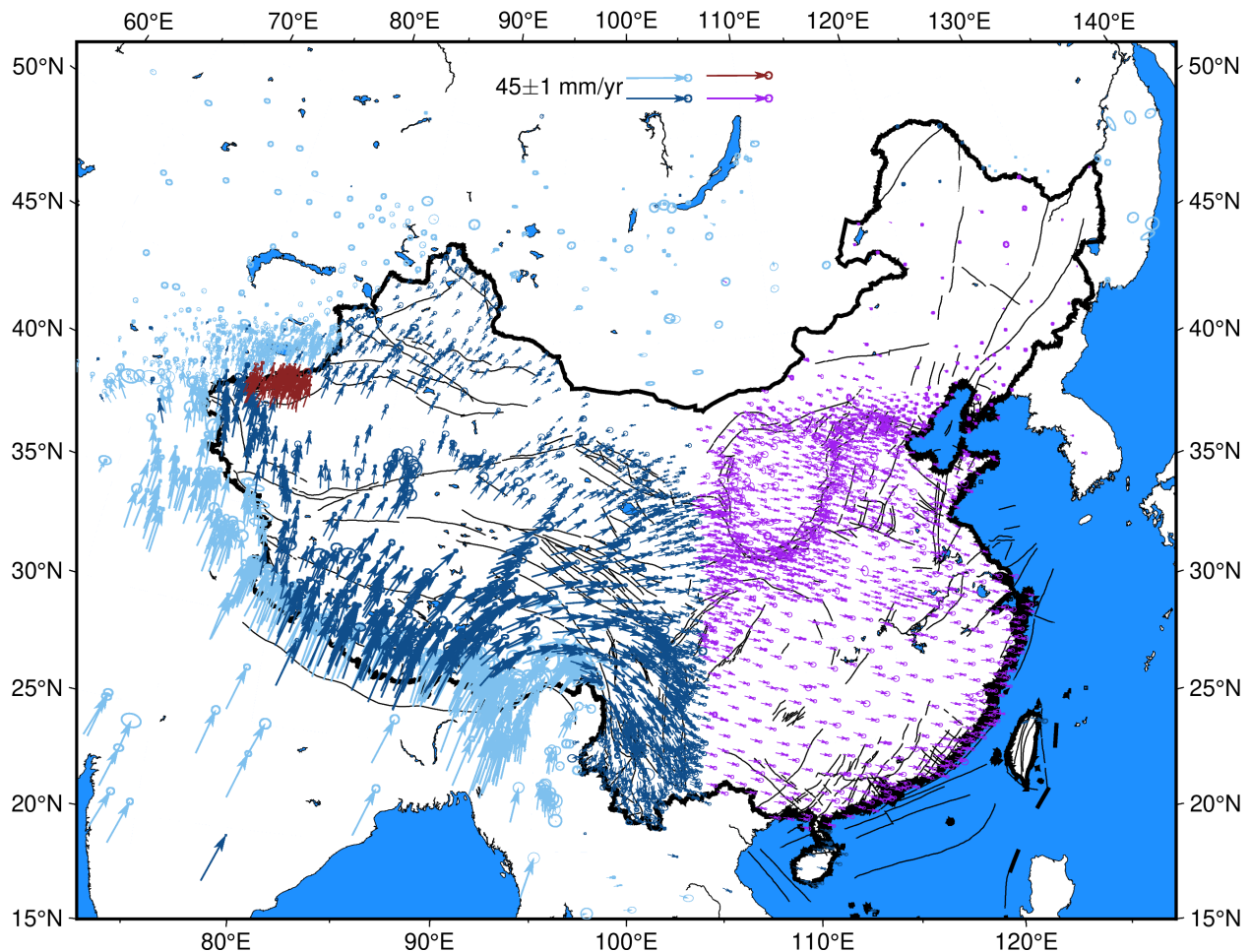
424 **Figure 9.** The Gradient of spherical harmonics with $l = 96, m = 48$ and fitting results of the
 425 spherical spline. (a) $\frac{dv_\varphi}{d\theta}$ calculated by spherical harmonics. (b) $\frac{dv_\varphi}{d\theta}$ fitted by spherical spline. (c)
 426 $\frac{dv_\theta}{d\theta}$ calculated by spherical harmonics. (d) $\frac{dv_\theta}{d\theta}$ fitted by spherical spline.

427 6 Seismic Mechanism and Strain Rate of Continental China

428 The Chinese mainland is an active geological tectonic area in a unique tectonic setting
 429 where the Eurasian Plate, Indian Plate, and Philippines Sea Plate meet in a triangular framework.
 430 As a result of the squeeze from India and the Philippine Sea Plate, earthquake in continental China
 431 is quite active. The M 7.8 earthquake in Tangshan in 1976 caused the death of 200,000 people;
 432 The M 8.1 earthquake in Hohxil in 2001 was the largest in China since 1960; The 2008 Wenchuan
 433 earthquake in Sichuan took nearly 70,000 lives and caused economic losses of almost 85 million
 434 RMB. Therefore, the study of seismic activity is of great importance to people's livelihoods and
 435 the economy. Studying the strain rate of the shallow ground is an essential reference for
 436 understanding the seismic mechanism.

437 The source of the GNSS velocity data we use is the same as in Section 4. In section 4, we
 438 only used the station locations. In contrast, in this section, we will use the measured GNSS velocity
 439 data to calculate the strain rate for continental China using the spherical spline method. Figure 10

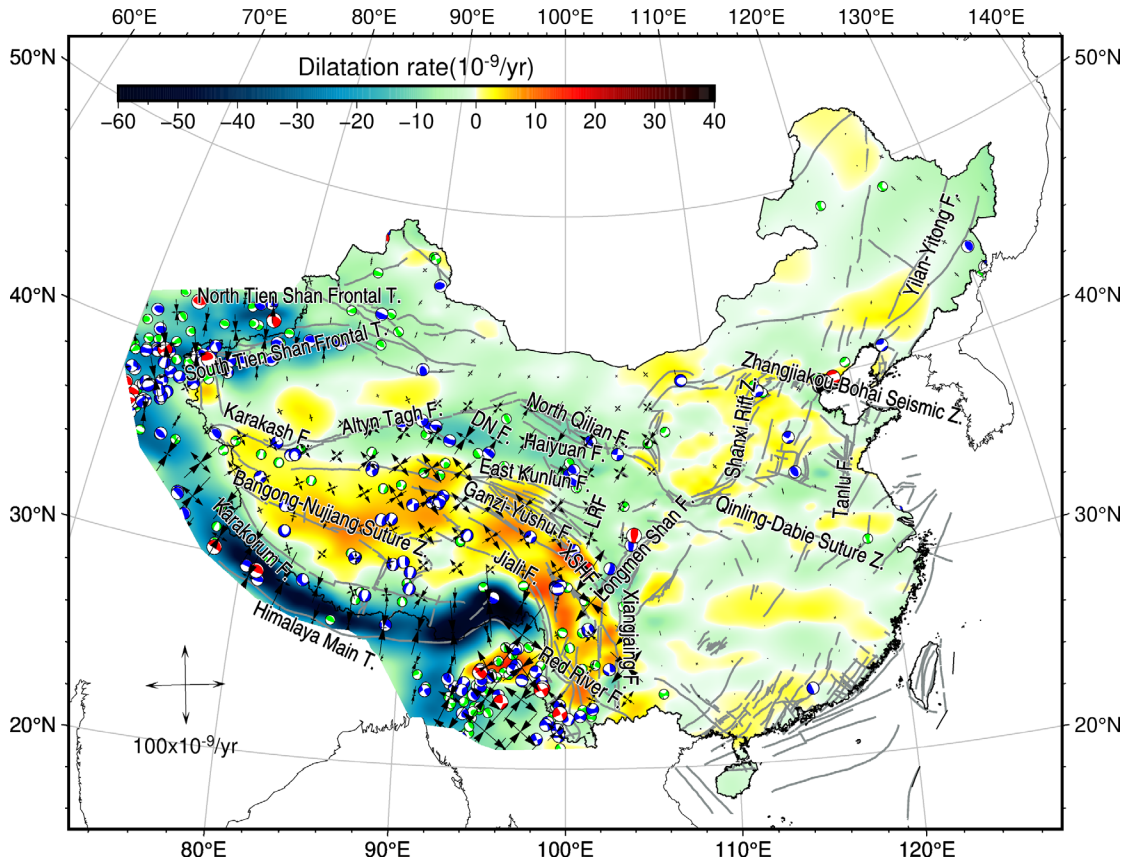
440 shows the velocity vector of all stations in continental China and its surroundings. For the accuracy
 441 of the calculation results, we excluded the data where the relative error of velocity components
 442 exceeded 10% and the relative error of velocity vector size exceeded 30%.



443
 444 **Figure 10.** GNSS velocity. The deep blue arrows are from Wang & Shen (2020); the light blue
 445 arrows are from Kreemer et al. (2014); the brown arrows are from Li et al. (2022); the purple
 446 arrows are from Wang et al. (2022). Wang et al. (2022) processed Ordos data from Hao et al. (2021)
 447 so that it would agree with the reference system and noise level of Wang & Shen (2020). We
 448 processed data from Li et al. (2022) using the same methodology. All GNSS velocity is listed in
 449 Table S1.

450 The background of Figure 11 shows the dilatation of continental China, whose negative is
 451 extrusion and the positive is tension. Due to the north-eastward extrusion of the Indian plate, the
 452 largest strain on the Chinese mainland is in the subduction zone of the Himalayan Main Thrust,
 453 where the dilatation rate exceeds $-40 \times 10^{-9}/\text{yr}$. On the eastern side of the Himalayan Main
 454 Thrust, the dilatation rate reaches about $-80 \times 10^{-9}/\text{yr}$, caused by the lateral extrusion of the
 455 Tibetan plateau being blocked by the SCB (Leigh H. Royden et al., 1997; Zhang et al., 2018;
 456 Zhang et al., 2004). The deformation of the Gan-Yushu Fault, XSHF, the Xiangjiang River Fault,
 457 and the Red River Fault region in the junction of the Tibetan Plateau and the SCB is to the vertical
 458 direction of the extrusion overflow and greater than the extrusion, so these areas generally exhibit
 459 a tensile nature (Bai et al., 2010; Zhao et al., 2022). We believe that it is also due to the lateral

460 extrusion of the Qinghai-Tibet Plateau caused by the South China plate blocking it from
461 overflowing in the vertical direction. The seismic mechanism can also explain this in this area
462 exhibiting strike-slip or normal fault. The interior of the Qinghai-Tibet Plateau may also be
463 vertically overflowing when squeezed, so the overall deformation is in tension. At the same time,
464 the seismic mechanism of this region can also indicate this. The northeastern and northern margin
465 of the Qinghai-Tibet Plateau is influenced by the far plant of the Indian plate extrusion, so this area
466 receives extrusion. Figure 11 demonstrates the extrusive nature of the fault system along the
467 northern and northeastern margins of the Tibetan Plateau, and the dilatation rate in this area is
468 between $-15 \times 10^{-9}/yr$ and $-20 \times 10^{-9}/yr$. Also affected by the compression of the Indian
469 plate is the Tianshan orogenic belt, which has a dilatation rate of $-40 \times 10^{-9}/yr$ at the subduction
470 front. At the same time, Figure 11 shows the extrusion strain zone in the eastward extension of
471 North and South Tianshan with a dilatation rate of $-10 \times 10^{-9}/yr$. The seismogenic mechanisms
472 of the northern and northeastern margins of the Qinghai-Tibet Plateau and the Tien Shan frontal
473 margin have been dominated by thrust faulting consistent with the dilatation rate results. And the
474 greater the magnitude of the dilatation rate, the more frequent the earthquakes. Seismic activity
475 and mechanism of western China are correlated with the dilatation rate. Reverse-fault earthquakes
476 frequently occur in regions with negative dilatation rates, and normal-fault or strike-slip
477 earthquakes occur in areas with positive dilatation rates. Although fewer large earthquakes exist
478 in Eastern China, the dilatation results also show this pattern. The Longmenshan Fault, located at
479 the junction of East and West China, is considerably squeezed, and t reverse-fault earthquakes
480 dominate the frequency of earthquakes in this area. However, positive fault earthquakes dominate
481 the East Kunlun F., Ganzi-Yushu F., and Jiali F. to the west. Figure 11 dilatation rate results clearly
482 show this pattern, indicating that our dilatation rate results possess high resolution. The dilatation
483 rate of the North China seismic zone in the East China region is relatively complex. The
484 intersection of the Zhangjiakou-Bohai seismic zone and the Tanlu Fault has the largest dilatation
485 rate, and the Tangshan earthquake occurred in this area in 1976. In addition, the number of large
486 earthquakes is also higher in this area than in the surrounding regions. The SCB is relatively stable
487 and has never experienced an earthquake of $M \geq 5.5$ since 1960 and the dilatation rate in this
488 region is close to zero.

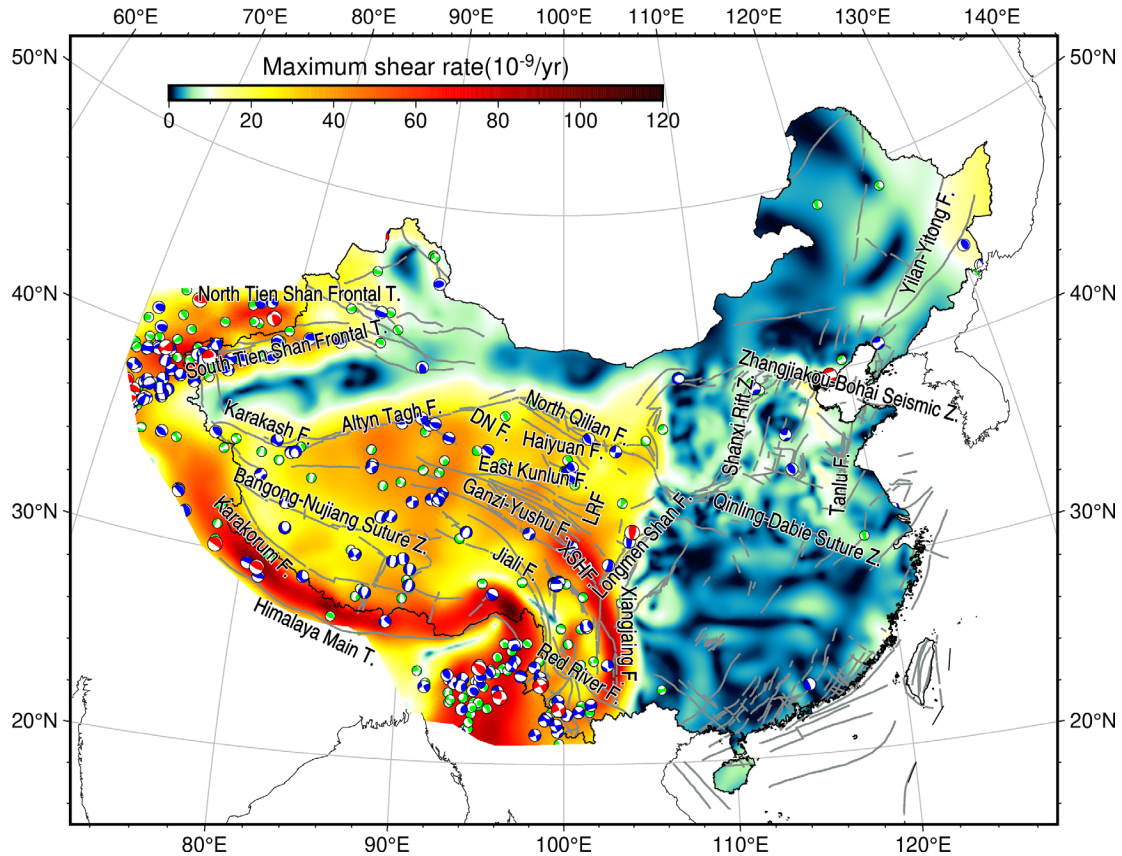


489

490 **Figure 11.** The dilatation rate of continental China. The gray lines on the background denote
 491 activity tectonic in continental China; The crossed arrows indicate the magnitude and direction of
 492 the maximum and minimum principal strains. The seismic mechanism in continental China from
 493 January 1, 1976, to December 31, 2021, is shown in the figure by the focal sphere. The red focal
 494 sphere indicates $M \geq 7.5$, the deep blue focal sphere indicates $7.5 \geq M \geq 6.5$, and the green focal
 495 sphere indicates $6.5 \geq M \geq 5.5$. Fault name abbreviations are as follows: DNF, Danghe-
 496 Nanshan Fault; LRF, Longriba Fault; XSHF, Xiashuihe Fault.

497 The background in Figure 12 shows the MSSR (maximum shear strain rate). We still see a
 498 clear division between East and West China along $105^\circ E$. MSSR is strongly correlated with
 499 earthquakes whose source mechanisms are strike-slip faults. In Figure 12, we can conclude that
 500 the areas with an MSSR greater than $40 \times 10^{-9}/yr$ are widely distributed on strike-slip faults and
 501 reverse-fault earthquakes. By the collisional compression of the Indian plate, the MSSR in
 502 continental China is greatest in the western and eastern sections of the HMT. Indian plate directly
 503 extrudes the eastern section of the Himalayas, and the MSSR reaches about $100 \times 10^{-9}/yr$.
 504 While the eastern section is rotated due to lateral extrusion from the Tibetan plateau, the MSSR
 505 reaches about $120 \times 10^{-9}/yr$. Longmenshan Fault, Xiangjiang Fault, and XSHF are located at
 506 the junction of Qinghai-Tibetan Plateau and SCB under great compression, and the MSSR has also
 507 reached $100 \times 10^{-9}/yr$. The MSSR of the North and South Tianshan Frontal Thrust, influenced
 508 by the far field of the Indian Plate extrusion, reaches about $70 \times 10^{-9}/yr$. In the northern and
 509 northeastern margins of the Tibetan Plateau, the MSSR show a clear boundary with the stable
 510 blocks in the north. In the areas where strike-slip earthquakes are widely developed in the interior
 511 of the Tibetan Plateau, the MSSR is more than $40 \times 10^{-9}/yr$. In East China, except for

512 Zhangjiakou-Bohai Seismic Zone and Yilan-Yitong Fault, the MSRR of other areas is very small
 513 and close to $10 \times 10^{-9}/\text{yr}$. The MSRR in most of Eastern China is very small, close to
 514 $10 \times 10^{-9}/\text{yr}$. Only ZBSZ and YYF have MSRR close to $40 \times 10^{-9}/\text{yr}$, and there is also some
 515 large earthquake distribution. Due to the special plate tectonics of the Chinese continent, the
 516 Tibetan Plateau is blocked by the surrounding rigid blocks as it expands outward under
 517 compression. All strain rate data are listed in Table S2-S4.



518
 519 **Figure 12.** The maximum shear rate of continental China. The gray lines on the background
 520 denote active tectonic in continental China. The seismic mechanism in continental China from
 521 January 1, 1960, to December 31, 2021, is shown in the figure by the focal sphere. The red focal
 522 sphere indicates $M \geq 7.5$, the deep blue focal sphere indicates $7.5 \geq M \geq 6.5$, and the green
 523 focal sphere indicates $6.5 \geq M \geq 5.5$ (same as Figure 11).

524 7 Discussions

525 7.1 Deformation and Strain Rates of Continental China

526 7.1.1 Overview of Continental China

527 Because of the multiscale spherical spline interpolation method, our dilatation rate results
 528 (Figure 11 and Figure 12) improve the resolution of the primary structure compared to the previous
 529 ones (Rui & Stamps, 2019; Wang & Shen, 2020). Continent China is located in the squeeze triangle
 530 of the Indian and Pacific plates and is extremely active in tectonic activities. We propose a concept
 531 named 10^{-8} Shear Zone to visualize the influence of the extrusion of these two plates on the

532 deformation of the entire Chinese continent, and we can observe this shear zone in Figure 12. The
533 central part of the 10^{-8} Shear Zone starts at Karakorum F. in the east, extends to ATF and NQF
534 (North Qianlian F.), and curves upward to Northwest Ordos. Then, this shear zone extends down
535 the western edge of the Ordos, passes through the Qinling Mountains, extends the Shanxi Rift Z.
536 on the eastern edge of the Ordos northward to Zhangjiakou, and finally extends the ZBSZ eastward
537 to the Bohai Sea. In addition, there are two other important branches of this shear zone. The first
538 branch extends to the junction of the Southern Tien Shan and the Tarim Basin, then northward in
539 the middle of the Southern Tien Shan to the middle of the Northern Tien Shan, dividing the entire
540 Northern and Southern Tien Shan into East and Western sections. This section of the branch shear
541 zone is connected to the main shear zone on the west side of KF (Karakash F.). Another branch
542 extends through LMSF (Longmen Shan F.) and XJF (Xiaojiang F.), joining the main shear zone
543 in southwest of Ordos. This branch also coincides with the boundary between the Tibetan Plateau
544 and South China. We can see that the tensile and compressive strains within the blocks around the
545 Tibetan Plateau, such as the Tarim block, the Alashan block, the Ordos block, and the South China
546 block, are small in Figure 11. At the same time, the maximum shear strains of these blocks are also
547 small in Figure 12, indicating that these blocks exhibit rigid body properties. But the effects of the
548 squeeze don't go away, with far-field effects affecting areas further afield. Tianshan's high shear
549 strain rate and high extrusion strain rate result from the influence of far-field benefits. Thus, in
550 western China and around the $105^{\circ}E$, the 10^{-8} Shear Zone mainly indicates the extent of influence
551 of the Indian subcontinent squeezing continental China. Although North China is affected by the
552 dual far-field effects of the Tibetan Plateau and the Pacific Plate, the 10^{-8} Shear Zone also indicates
553 their influence. This shear zone provides visual evidence of the extent to which localized
554 deformation in continental China is affected by plate extrusion and avoids attributing deformations
555 whose causes are unclear to plate extrusion or its far-field effects.

556 7.1.2 Deformation of Tibetan Plateau

557 The Tibetan Plateau is inevitably one of continental China's most dramatic active tectonics.
558 The thickening, shortening, and lateral extrusion of the Tibetan Plateau under the compression of
559 the Indian plate and the blocking of surrounding blocks is noticeable and almost indisputable (Gan
560 et al., 2007). However, whether crustal thickening or lateral extrusion played a major role in
561 balancing the plateau's uplift is still controversial. An accurate description of the deformation of
562 the Tibetan Plateau is therefore essential for clarifying these issues. There have been many
563 deformation studies based on GPS velocity fields, and researchers customarily use relative velocity
564 models to delineate microplates and account for their interactions. It may sometimes neglect the
565 overall deformation, so it is more reasonable to use strain rates composed of velocity gradients
566 because the velocity gradient does not vary with the reference system. The microplates of the
567 Tibetan Plateau have been carefully delineated in recent years (Loveless & Meade, 2011; Meade,
568 2007; Thatcher, 2007; Wang et al., 2017), the microplate model and the continuum deformation
569 model have been harmonized. Rotation has always been a concern in microplate modeling. From
570 our strain rate results, we can get that the internal deformation properties of the Tibetan Plateau
571 tend to be consistent, and the drastic changes in values and properties are mainly at the edge of the
572 Tibetan Plateau. Wang et al. (2017) used the GPS velocity field and microplate model to obtain
573 that the southwestern part of the Tibetan Plateau shows a counterclockwise rotation, the
574 southeastern part shows a clockwise rotation, the Tsaidam Basin shows a clockwise rotation, and
575 the middle part of the Himalaya shows a counterclockwise rotation. In Figure S9, we offer the
576 results of the rotational strain rate where positive values indicate counterclockwise and negative

577 values indicate clockwise. My results generally agree with the nature of Wang et al. (2017) in the
578 southwestern and northeastern Tibetan Plateau, and the nature of the rotation in the Tsaidam Basin
579 and the middle Himalayas is opposite to his results. But our results are identical to those of Ge et
580 al. (2015) and Wang & Shen (2020). Wang et al. (2017) use Ma as the unit of time, and the rotation
581 values in the regions that do not agree with our results are smaller, so there may be some errors in
582 the statistics and calculations. Thus, it follows from our rotational strain rate model that the interior
583 of the Tibetan Plateau may not need to be divided into many microplates to explain deformation.
584 We can see from Fig. 2 that the resolution of our strain rate model on the Tibetan Plateau reaches
585 110 km at the largest spatial scale (scale factor $q \geq 6$, The larger the scale factor, the higher the
586 resolution), which can fully satisfy the current microplate scale. Of course we don't fully support
587 this model of the Tibetan Plateau as a whole piece. Because our results support the traditional
588 delineation of land parcels bounded by large active tectonics. In Fig. 12, we see the variation of
589 the MSSR on both sides of the BNF to distinguish the Lhasa block from the Qiangtang block. In
590 Fig. 11, we see a change in the nature of the tensile on either side of the EKF (East Kunlun F.) to
591 distinguish the Songpan-Ganzi Block from the Qiangtang Block. There is also a clear zone of high
592 extrusion in the middle of the Qaidam Basin and the Songpan-Ganzi Block. So how can researchers
593 improve the accuracy of numerical experiments to explain the crustal deformation of the Tibetan
594 Plateau without microplates? We believe that it is possible to improve the resolution of the elastic
595 parameters of the material. Our study has given high-resolution strain rates, and high-resolution
596 continuous elastic parameters can be obtained after simple calculations using the Hooke's law (All
597 strain rate data are listed in Table S2-S4). Numerical modeling in conjunction with current plate
598 delineation based on large active ruptures may have been able to give better results.

599 Another deformation of interest is a crustal circulation channel on the eastern Tibetan
600 Plateau and where it begins and ends. Many researchers believe that the Tibetan Plateau, as it
601 extrudes laterally to the east, is blocked by the tough Sichuan Basin to form northward and
602 southward branches. Branching to the north extends to the RRF (Red River F.), and branching to
603 the east rises to the edge of the Ordos block (Bai et al., 2010; Bao et al., 2015; Zhang et al., 2020).
604 The existence of lower and middle crustal flows has been confirmed by much geophysical
605 observational evidence on the northeast Tibetan Plateau, such as the hyperthermal layer (Deng &
606 Tesauro, 2016; Jiang et al., 2019), the lower and middle crustal low-resistive layers (Zhao et al.,
607 2012), distribution of epicenter depths (Liang et al., 2008; Wang et al., 2020; Wei et al., 2010) and
608 the anisotropy of the crust (Kong et al., 2016; Zheng et al., 2018). There is no evidence of a
609 lubricating or decoupling layer between the lower and middle crust and the upper crust. Therefore,
610 the deformation of the lower and middle crust should be consistent with that of the upper crust. In
611 figure 11, our results show that the crustal flow in the southeastern Tibetan Plateau is divided into
612 two streams, the first one extending from Ganzi-Yushu F., XSHF to XJF., and the other extending
613 from Jiali F. to RRF. It is consistent with the current study. It is also surface observational evidence
614 for the existence of crustal flows. In addition, our results show that the two crustal flow channels
615 are connected near XSHF and XJF. However, our dilatation rates result do not show the effect of
616 crustal flow on the surface in the northeastern Tibetan Plateau, and only the northeastern portion
617 of the Tibetan Plateau showed slightly higher maximum shear rates. It may suggest no large-scale
618 crustal flow in the northeastern Tibetan Plateau or a lubricating layer between the lower and middle
619 crust and the upper crust. Even if there was crustal flow, it didn't spread to the edge of the Ordos
620 Block.

621 7.1.3 Deformation of North China in Continental China

622 North China is another region of high seismicity in mainland China, where the deformation
623 and dynamics of the region are of great interest because of the large population and industrial bases
624 and the extrusion of both the eastern side of the Tibetan Plateau and the western Pacific Plate.
625 Figure S9 shows details of strain rates in North China. Our maximum strain rates are similar to the
626 results obtained by the most recent modeling approach using elastic-plastic layering (Shen et al.,
627 2023). The MSSR at the northern edge of the Ordos block is smaller than the other boundaries,
628 showing a semi-enveloped morphology. The MSSR at the northern edge of the Ordos Block is
629 smaller than the different boundaries. It suggests a longer recurrence cycle of strong earthquakes
630 in northern Ordos. Our results differ from Shen et al. (2023) in areas where strain is concentrated.
631 In Figure S10, the eastern part of the Zhangjiakou-Bohai Seismic Zone, where the Tangshan
632 earthquake occurred, is a strain rates concentration area with short recurrence periods of strong
633 earthquakes requiring focused monitoring. In addition, the areas of relatively large strain rates in
634 the North China block are concentrated around the active tectonics, including the Shanxi Rift Z.,
635 Anyang-Heze-Linyi F., Weihe Rift, and THCF (Tang Shan-Hejian-Cixian F.). At the boundary
636 between North and South China, Qinling-Dabie Suture Z., there is no stress concentration, and our
637 results are consistent with Shen et al. (2023) and seismological perception (Yu & Chen, 2016).
638 However, we used more intensive measured data to obtain a strain rate model with higher
639 resolution, which also supports the current dominant block models (DENG et al., 2003; Wang et
640 al., 2022; Yin et al., 2015). Thus, our results may be more plausible.

641 The 10^{-8} shear zone is still in effect in North China, and this zone extends to the THCF
642 and the Tanlu Fault, suggesting that these two active tectonic structures are the concentration of
643 strain in North China as a result of the extrusion of the Tibetan Plateau and the Pacific Plate.

644 7.2 Seismic Activity and Strain Rates of Continental China

645 As mentioned earlier in our study, Figure 11 demonstrates that dilatation is highly
646 consistent with the source mechanism of $M \geq 5.5$ earthquakes. Figure 12 demonstrates the
647 agreement of the MSSR with earthquakes on strike-slip faults of $M \geq 5.5$. In addition, there are
648 no major earthquakes in areas where the dilatation rate or the MSSR is anomalous. We consider
649 these areas with abnormal strain rate values as earthquake warning areas. In Figure 11, the
650 dilatation rate along the ATF is approximately $-20 \times 10^{-8}/yr$, and only the western section of
651 the ATF is more seismically intense. In Figure 12, The small MSRR in the east section of the
652 ATF may be why there are fewer large earthquakes in this region. The eastern section of TSFT
653 (TianShan Frontal T.) and the eastern section of the ATF have the same strain rate and seismic
654 distribution characteristics, and this feature is also found in the triangle enclosed by LRF
655 (Longriba F.), XSHF, and LMSF. Although Figures 11 and 12 show that the NQF has this
656 feature again, that is because of the absence of data on the seismic mechanism, and we know
657 from Figure 10 that there is a large distribution of earthquakes in this area. Although the
658 dilatation rate of the western edge of the Ordos block is low, the MSRR is large, especially since
659 the intersection with NQF has the possibility of large earthquakes. The distribution of only a few
660 earthquakes $M \geq 5.5$ in northern China is consistent with the distribution of high values of the
661 dilatation rate and the MSRR, and these areas remain of concern.

662 7.3 Spherical Spline Method

663 The spherical spline can directly give a derivative of GNSS velocity, which does not
664 depend on the fitting result of the velocity field. Furthermore, the spherical harmonics detection

665 model shows numerical stability with a large velocity gradient. However, the maximum order and
666 degree of spherical harmonics we use are 96 and 48. We also obtain the ideal results using bigger
667 orders and degrees' spherical harmonics detection model. We observe that there is one station data
668 at the edge of a grid, then this side of the edge of the grid will recover the value sign (positive and
669 negative) of the grid where it is located. (e.g., Figures 5 and 7).

670 As we mentioned at the beginning of this article, we have developed a set of test criteria to
671 judge whether some methods of calculating strain rate using GPS or GNSS velocity are effective.
672 The criteria do not target spherical spline mainly. In geophysical and geodynamic research, the
673 effectiveness of fitting or smoothing using a different method for the same discrete data has some
674 visible discrepancies. However, only some methods perform well within a large study area. Some
675 methods are better than others in local areas, which is also the principal aspect discussed by
676 researchers when they select fitting or smoothing methods. We present a spherical harmonics grid
677 inspection model by analogy with a seismic wave velocity checkboard test. Using spherical
678 harmonics with a grid distribution feature, we can judge the overall fitting effect of a strain rate
679 calculating method in the study area and consider the local detail resolution of the technique. Even
680 if the same data is used, different methods have different local resolutions, so higher-resolution
681 methods can also be an option in other parts of a larger study area.

682 Of course, the way to solve the interpolation accuracy and to get a better smoothing effect
683 is to increase the station density locally. However, refining stations in all areas, regardless of cost,
684 is not conducive to cost savings and efficiency, so we use the spherical harmonic grid test model
685 to determine whether the distribution of stations in the study target area is reasonable and improved.
686 We take the station density distribution in continental China as an example. From the results of
687 the spherical harmonic lattice test of the spherical strip, it is necessary to increase the stations in
688 the rectangular area from $32^{\circ}N$ to $37^{\circ}N$, $81^{\circ}E$ to $92^{\circ}E$. This area has experienced major
689 earthquakes and is in the Tibetan hinterland, a famous no-man's land. However, the deformation
690 mechanism within the Qinghai-Tibet Plateau is still unclear. Based on the spherical spline results,
691 it is unnecessary to deploy stations intensively, but only to add 3-5 stations over a wide range area
692 to significantly improve the resolution of strain rate results. In addition, the spherical harmonic
693 test also shows that adding two or three stations in the hinterland of the Qaidam Basin and the
694 Alashan massif is also beneficial to improving the computational accuracy of the north-south
695 derivatives (which is mainly related to $\dot{\epsilon}_{\varphi}$). Refining station in other areas is practically
696 unnecessary.

697 No matter what method or data is used, data can be filtered, and methods can be chosen
698 differently, but the study area is permanently fixed. Although we recommend using different
699 methods in different regions in the previous section, using various methods locally in a fixed study
700 area may have some continuity problems on the boundaries. Moreover, in the last quarter, we
701 mentioned that spherical coordinates are more reliable at high latitudes (e.g., Iceland) or in a large
702 study area at low latitudes (e.g., continental China). Jiang *et al.* (2011) concluded that the least-
703 squares collocation method in spherical coordinates is superior to other methods. However, the
704 least-squares collocation method is based on first-order Taylor expansions of displacement or
705 velocity fields in the spherical and Cartesian coordinate systems. It is like linear interpolation,
706 which can only guarantee the continuity of the strain rate but not the smoothness. This method is
707 reasonable when the stations are dense, but when the stations are sparse, the calculation results are
708 not guaranteed to be practical. Therefore, in addition to proposing a set of test criteria for the strain
709 rate method, this paper also recommends that researchers use the spherical spline method, which

710 is not only a high-precision spherical coordinate method but also ensures continuous and smooth
711 strain rate results.

712 **8 Conclusions**

713 We propose a set of criteria to test the practicality of calculating strain or strain rate fields
714 using GPS or GNSS data. This set of standards is also illustrated using the spherical spline method
715 utilizing the location of stations in and around continental China.

716 The final three main conclusions drawn in this paper are

717 (1) Unlike the Cartesian coordinate method, the spherical coordinate method can be
718 adapted to examine rigid body rotation models and reduce the error to less than one percent or
719 even one thousandth. The spherical harmonic grid model is designed to visualize the method's
720 resolution. We can use different sizes and shapes of spherical harmonic grids to examine our strain
721 rate calculation methods rather than just the spherical spline method used in this paper.

722 (2) The 10^{-8} reveals the extent to which the Chinese mainland is affected by the extrusion
723 of the Indian plate and the extrusion of the Pacific plate. This zone is also valid in North China.

724 (3) It may be more reasonable to explain the deformation mechanism of the Tibetan Plateau
725 using a continuum model. At the same time, the high-resolution strain rate we provide helps to
726 obtain continuous high-resolution elastic parameters.

727 (4) We provide strain rate evidence for the distribution of lower and middle crustal flows
728 on the southeastern Tibetan Plateau and inform the connectivity of the two side channels.

729 (5) The region of high shear strain rate in North China overlaps with the microplate margins
730 delineated by active fault. However, Tangshan is still the region with the highest MSRR and the
731 dilation rate, which needs to be highly emphasized.

732 (6) The dilatation rate and the MSRR calculated using the spherical spline method have an
733 excellent performance in analyzing the seismic mechanisms of faults or earthquakes. It is
734 recommended that other researchers use the spherical spline method when analyzing the seismic
735 mechanism. Attention must be focused on areas with large dilatation rates and MSRR, especially
736 those anomalous compared to the surrounding areas with a high potential for future major
737 earthquakes.

738 **Acknowledgments**

739 This research is supported by the National Science Foundation of China (U2239205, 41725017)

740 and the National Key R&D Program of the Ministry of Science and Technology of China

741 (2020YFA0713401). It is also partially supported by the National Key Scientific and

742 Technological Infrastructure project "Earth System Science Numerical Simulator Facility"

743 (EarthLab). All the authors greatly appreciate Professor Carl Tape for providing the software

744 package to us.

745 **Open Research**

746 The GNSS data used in this study were taken from published papers (Li et al., 2022; Wang & Shen,
747 2020; Wang et al., 2022) and are listed in Table S1. The GNSS velocity and strain rate data are
748 published to Zenodo (<https://zenodo.org/records/10215151>). Earthquake Catalog was obtained from
749 USGS (United States Geological Survey)
750 ([https://earthquake.usgs.gov/fdsnws/event/1/query.csv?starttime=1960-01-
751 01%2000:00:00&endtime=2021-12-
752 31%2023:59:59&maxlatitude=55.479&minlatitude=15.824&maxlongitude=138.516&minlongitude=69
753 .082&minmagnitude=5.5&orderby=time](https://earthquake.usgs.gov/fdsnws/event/1/query.csv?starttime=1960-01-01%2000:00:00&endtime=2021-12-31%2023:59:59&maxlatitude=55.479&minlatitude=15.824&maxlongitude=138.516&minlongitude=69.082&minmagnitude=5.5&orderby=time)). The seismic mechanism data were obtained from the
754 Global Centroid Moment Tensor (Dziewonski et al., 2012; Ekström et al., 2012)
755 ([https://www.globalcmt.org/cgi-bin/globalcmt-cgi-
756 bin/CMT5/form?itype=yymd&yr=1976&mo=1&day=1&otype=yymd&oyr=2021&omo=12&oday=31&jyr=
757 1976&jday=1&ojyr=1976&ojday=1&nday=1&lmw=5.5&umw=10&lms=0&ums=10&lmb=0&umb=10&ll
758 at=15&ulat=55&llon=70&ulon=140&lhd=0&uhd=1000<s=-
759 9999&uts=9999&lpe1=0&upe1=90&lpe2=0&upe2=90&list=6](https://www.globalcmt.org/cgi-bin/globalcmt/cgi-bin/CMT5/form?itype=yymd&yr=1976&mo=1&day=1&otype=yymd&oyr=2021&omo=12&oday=31&jyr=1976&jday=1&ojyr=1976&ojday=1&nday=1&lmw=5.5&umw=10&lms=0&ums=10&lmb=0&umb=10&lat=15&ulat=55&llon=70&ulon=140&lhd=0&uhd=1000<s=-9999&uts=9999&lpe1=0&upe1=90&lpe2=0&upe2=90&list=6)).

760 **Reference**

761 Backus, G. (1967). Numerical applications of a formalism for geophysical inverse problems.
762 *Geophysical Journal International*, 13(1-3), 247-276. doi: 10.1111/j.1365-246X.1967.tb02159.x
763 Backus, G. (1968). The resolving power of gross earth data. *Geophysical Journal International*,
764 16(2), 169-205. doi: 10.1111/j.1365-246X.1968.tb00216.x
765 Backus, G. (1970). Uniqueness in the inversion of inaccurate gross earth data. *Royal Society*,
766 266(1173), 123-192. doi: 10.1098/rsta.1970.0005
767 Bai, D., Unsworth, M. J., Meju, M. A., Ma, X., Teng, J., Kong, X., et al. (2010). Crustal
768 deformation of the eastern Tibetan plateau revealed by magnetotelluric imaging. *Nature*
769 *Geoscience*, 3(5), 358-362. doi: 10.1038/ngeo830

- 770 Bao, X., Sun, X., Xu, M., Eaton, D. W., Song, X., Wang, L., et al. (2015). Two crustal low-
771 velocity channels beneath SE Tibet revealed by joint inversion of Rayleigh wave dispersion and
772 receiver functions. *Earth and Planetary Science Letters*, *415*, 16-24. doi:
773 Bürgmann, R. (2005). Interseismic coupling and asperity distribution along the Kamchatka
774 subduction zone. *Journal of Geophysical Research*, *110*(B7), B07405. doi:
775 10.1029/2005jb003648
- 776 Chen, Q., Freymueller, J. T., Yang, Z., Xu, C., Jiang, W., Wang, Q., & Liu, J. (2004). Spatially
777 variable extension in southern Tibet based on GPS measurements. *Journal of Geophysical*
778 *Research: Solid Earth*, *109*(B9), n/a-n/a. doi: 10.1029/2002jb002350
- 779 Day, A. J., Peirce, C., & Sinha, M. C. (2001). Three - dimensional crustal structure and magma
780 chamber geometry at the intermediate - spreading, back - arc Valu Fa Ridge, Lau Basin—results
781 of a wide - angle seismic tomographic inversion. *Geophysical Journal International*, *146*(1), 31-
782 52. doi: 10.1046/j.0956-540X.2001.01446.x
- 783 DENG, Q., ZHANG, P., RAN, Y., YANG, X., MIN, W., & CHU, Q. (2003). Basic
784 characteristics of active tectonics of China. *Science in China Series D-Earth Sciences*, *46*(4),
785 356-372. doi: 10.1360/03yd9032
- 786 Deng, Y., & Tesauro, M. (2016). Lithospheric strength variations in Mainland China: Tectonic
787 implications. *Tectonics*, *35*(10), 2313-2333. doi: 10.1002/2016tc004272
- 788 Devachandra, M., Kundu, B., Catherine, J., Kumar, A., & Gahalaut, V. K. (2014). Global
789 Positioning System (GPS) Measurements of Crustal Deformation across the Frontal Eastern
790 Himalayan Syntaxis and Seismic - Hazard Assessment. *Bulletin of the Seismological Society of*
791 *America*, *104*(3), 1518-1524. doi: 10.1785/0120130290

- 792 Dziewonski, A. M., Chou, T. A., & Woodhouse, J. H. (2012). Determination of earthquake
793 source parameters from waveform data for studies of global and regional seismicity. *Journal of*
794 *Geophysical Research: Solid Earth*, 86(B4), 2825-2852. doi: 10.1029/JB086iB04p02825
- 795 Ekström, G., Nettles, M., & Dziewoński, A. M. (2012). The global CMT project 2004–2010:
796 Centroid-moment tensors for 13,017 earthquakes. *Physics of the Earth and Planetary Interiors*,
797 200-201, 1-9. doi: 10.1016/j.pepi.2012.04.002
- 798 Franklin, J. N. (1970). Well-posed stochastic extensions of ill-posed linear problems. *Journal of*
799 *Mathematical Analysis and Applications*, 31(3), 682-716. doi: 10.1016/0022-247X(70)90017-X
- 800 Gan, W., Zhang, P., Shen, Z.-K., Niu, Z., Wang, M., Wan, Y., et al. (2007). Present-day crustal
801 motion within the Tibetan Plateau inferred from GPS measurements. *Journal of Geophysical*
802 *Research*, 112(B8), B08416. doi: 10.1029/2005jb004120
- 803 Ge, W.-P., Molnar, P., Shen, Z.-K., & Li, Q. (2015). Present-day crustal thinning in the southern
804 and northern Tibetan Plateau revealed by GPS measurements. *Geophysical Research Letters*,
805 42(13), 5227-5235. doi: 10.1002/2015gl064347
- 806 Ge, W.-P., Wang, M., Shen, Z. K., Yuan, D. Y., & Zheng, W. J. (2013). Intersiesmic kinematics
807 and information patterns on the upper crust of Qaidan-Qilianshan block. *Chinese J. Geophys. (in*
808 *Chinese)*, 56(09), 2994-3010. doi: 10.6038/cjg20130913
- 809 Ge, W. P., Shen, Z. K., Molnar, P., Wang, M., Zhang, P. Z., & Yuan, D. Y. (2022). GPS
810 Determined Asymmetric Deformation Across Central Altyn Tagh Fault Reveals Rheological
811 Structure of Northern Tibet. *Journal of Geophysical Research: Solid Earth*, 127(9). doi:
812 10.1029/2022jb024216

- 813 Glahn, A., Granet, M., & Group, R. G. T. (1993). Southern Rhine Graben: small-wavelength
814 tomographic study and implications for the dynamic evolution of the graben. *Geophysical*
815 *Journal International*, 113(2), 399-418. doi: 10.1111/j.1365-246X.1993.tb00896.x
- 816 Graeber, F. M., Houseman, G. A., & Greenhalgh, S. A. (2002). Regional teleseismic tomography
817 of the western Lachlan Orogen and the Newer Volcanic Province, southeast Australia.
818 *Geophysical Journal International*, 149(2), 249-266. doi: 10.1111/j.1365-246X.1993.tb00896.x
- 819 Hao, M., Li, Y., & Zhuang, W. (2019). Crustal movement and strain distribution in East Asia
820 revealed by GPS observations. *Scientific Reports*, 9(1), 16797. doi: 10.1038/s41598-019-53306-y
- 821 Hao, M., Wang, Q., Zhang, P., Li, Z., Li, Y., & Zhuang, W. (2021). “Frame Wobbling” Causing
822 Crustal Deformation Around the Ordos Block. *Geophysical Research Letters*, 48(1). doi:
823 10.1029/2020gl091008
- 824 Hori, M., Kameda, T., & Kato, T. (2001). Application of the inversion method to a GPS network
825 for estimating the stress increment in Japan. *Geophysical Journal International*, 144(3), 597-608.
826 doi: 10.1046/j.1365-246x.2001.01337.x
- 827 Jiang, G., Hu, S., Shi, Y., Zhang, C., Wang, Z., & Hu, D. (2019). Terrestrial heat flow of
828 continental China: Updated dataset and tectonic implications. *Tectonophysics*, 753, 36-48. doi:
829 10.1016/j.tecto.2019.01.006
- 830 Jiang, G., Xu, C., Wen, Y., Xu, X., Ding, K., & Wang, J. (2014). Contemporary tectonic
831 stressing rates of major strike-slip faults in the Tibetan Plateau from GPS observations using
832 Least-Squares Collocation. *Tectonophysics*, 615-616, 85-95. doi: 10.1016/j.tecto.2013.12.022
- 833 Jiang, Z.-S., & Liu, J.-N. (2010). The method for establishing strain field and velocity field of
834 crustal movement using least squares collocation. *Chinese J. Geophys. (in Chinese)*, 53(05),
835 1109+1116-1117. doi: doi.org/10.1002/cjg2.1507

- 836 Kong, F., Wu, J., Liu, K. H., & Gao, S. S. (2016). Crustal anisotropy and ductile flow beneath
837 the eastern Tibetan Plateau and adjacent areas. *Earth and Planetary Science Letters*, *442*, 72-79.
838 doi:
- 839 Kreemer, C., Blewitt, G., & Klein, E. C. (2014). A geodetic plate motion and Global Strain Rate
840 Model. *Geochemistry, Geophysics, Geosystems*, *15*(10), 3849-3889. doi: 10.1002/2014gc005407
- 841 Lancaster, P., & Salakauskas, K. (1986). *Curve and Surface Fitting, an Introduction*: Academic
842 Press.
- 843 Lanza, F., Thurber, C. H., Syracuse, E. M., Power, J. A., & Ghosh, A. (2020). Seismic
844 tomography of compressional wave velocity and attenuation structure for Makushin Volcano,
845 Alaska. *Journal of Volcanology and Geothermal Research*, *393*, 106804. doi:
846 10.1016/j.jvolgeores.2020.106804
- 847 Leigh H. Royden, B. Clark Burchfiel, Robert W. King, Erchie Wang, Zhiliang Chen, Feng Shen,
848 & Liu, Y. (1997). Surface Deformation and Lower Crustal Flow in Eastern Tibet. *Science*, *276*.
849 doi: 10.1126/science.276.5313.788
- 850 Li, H., Li, S., Song, X. D., Gong, M., Li, X., & Jia, J. (2012). Crustal and uppermost mantle
851 velocity structure beneath northwestern China from seismic ambient noise tomography.
852 *Geophysical Journal International*, *188*(1), 131-143. doi: 10.1111/j.1365-246X.2011.05205.x
- 853 Li, J., Yao, Y., Li, R., Yusan, S., Li, G., Freymueller, J. T., & Wang, Q. (2022). Present - Day
854 Strike - Slip Faulting and Thrusting of the Kepingtage Fold - and - Thrust Belt in Southern
855 Tianshan: Constraints From GPS Observations. *Geophysical Research Letters*, *49*(11). doi:
856 10.1029/2022gl099105

- 857 Li, K., Li, Y., Tapponnier, P., Xu, X., Li, D., & He, Z. (2021). Joint InSAR and Field Constraints
858 on Faulting During the Mw 6.4, July 23, 2020, Nima/Rongma Earthquake in Central Tibet.
859 *Journal of Geophysical Research: Solid Earth*, 126(9). doi: 10.1029/2021jb022212
- 860 Liang, S., Gan, W., Shen, C., Xiao, G., Liu, J., Chen, W., et al. (2013). Three - dimensional
861 velocity field of present - day crustal motion of the Tibetan Plateau derived from GPS
862 measurements. *Journal of Geophysical Research: Solid Earth*, 118(10), 5722-5732. doi:
863 10.1002/2013JB010503
- 864 Liang, X., Zhou, S., Chen, Y. J., Jin, G., Xiao, L., Liu, P., et al. (2008). Earthquake distribution
865 in southern Tibet and its tectonic implications. *Journal of Geophysical Research: Solid Earth*,
866 113(B12). doi:
- 867 Liu, M., Yang, Y., Shen, Z., Wang, S., Wang, M., & Wan, Y. (2007). Active tectonics and
868 intracontinental earthquakes in China: The kinematics and geodynamics. In *Continental*
869 *Intraplate Earthquakes: Science, Hazard, and Policy Issues*.
- 870 Loveless, J. P., & Meade, B. J. (2010). Geodetic imaging of plate motions, slip rates, and
871 partitioning of deformation in Japan. *Journal of Geophysical Research*, 115(B2), B02410. doi:
872 10.1029/2008jb006248
- 873 Loveless, J. P., & Meade, B. J. (2011). Partitioning of localized and diffuse deformation in the
874 Tibetan Plateau from joint inversions of geologic and geodetic observations. *Earth and*
875 *Planetary Science Letters*, 303(1-2), 11-24. doi: 10.1016/j.epsl.2010.12.014
- 876 Masson, F., Lehujeur, M., Ziegler, Y., & Doubre, C. (2014). Strain rate tensor in Iran from a new
877 GPS velocity field. *Geophysical Journal International*, 197(1), 10-21. doi: 10.1093/gji/ggt509
- 878 Meade, B. J. (2007). Present-day kinematics at the India-Asia collision zone. *Geology*, 35(1).
879 doi: 10.1130/g22924a.1

- 880 Métois, M., Socquet, A., & Vigny, C. (2012). Interseismic coupling, segmentation and
881 mechanical behavior of the central Chile subduction zone. *Journal of Geophysical Research:*
882 *Solid Earth*, 117(B3), B03406. doi: 10.1029/2011jb008736
- 883 Okazaki, T., Fukahata, Y., & Nishimura, T. (2021). Consistent estimation of strain-rate fields
884 from GNSS velocity data using basis function expansion with ABIC. *Earth, Planets and Space*,
885 73(1). doi: 10.1186/s40623-021-01474-5
- 886 Pang, Y., Wu, Y., Li, Y., & Chen, C. (2023). The mechanism of the present-day crustal
887 deformation in southeast Tibet: from numerical modelling and geodetic observations.
888 *Geophysical Journal International*, 235(1), 12-23. doi: 10.1093/gji/ggad200
- 889 Qi, W., Xuejun, Q., Qigui, L., Freymueller, J., Shaomin, Y., Caijun, X., et al. (2011). Rupture of
890 deep faults in the 2008 Wenchuan earthquake and uplift of the Longmen Shan. *Nature*
891 *Geoscience*, 4(9), 634-640. doi: 10.1038/ngeo1210
- 892 Qu, W., Lu, Z., Zhang, Q., Wang, Q., Hao, M., Zhu, W., & Qu, F. (2018). Crustal deformation
893 and strain fields of the Weihe Basin and surrounding area of central China based on GPS
894 observations and kinematic models. *Journal of Geodynamics*, 120, 1-10. doi:
895 10.1016/j.jog.2018.06.003
- 896 Rawlinson, N., Salmon, M., & Kennett, B. L. (2014). Transportable seismic array tomography in
897 southeast Australia: Illuminating the transition from Proterozoic to Phanerozoic lithosphere.
898 *Lithos*, 189, 65-76. doi: 10.1016/j.lithos.2013.06.001
- 899 Rui, X., & Stamps, D. S. (2019). A Geodetic Strain Rate and Tectonic Velocity Model for China.
900 *Geochemistry, Geophysics, Geosystems*, 20(3), 1280-1297. doi: 10.1029/2018gc007806

- 901 Savage, J. C., Gan, W., & Svarc, J. L. (2001). Strain accumulation and rotation in the Eastern
902 California Shear Zone. *Journal of Geophysical Research: Solid Earth*, *106*(B10), 21995-22007.
903 doi: 10.1029/2000jb000127
- 904 She, Y., & Fu, G. (2020). Uplift Mechanism of the Highest Mountains at Eastern Himalayan
905 Syntaxis Revealed by In Situ Dense Gravimetry. *Geophysical Research Letters*, *47*(22). doi:
906 10.1029/2020gl091208
- 907 Shen, F., Wang, L., Barbot, S., & Xu, J. (2023). North China as a mechanical bridge linking
908 Pacific subduction and extrusion of the Tibetan Plateau. *Earth and Planetary Science Letters*,
909 *622*. doi: 10.1016/j.epsl.2023.118407
- 910 Shen, Z.-K., Jackson, D. D., & Ge, B. X. (1996). Crustal deformation across and beyond the Los
911 Angeles basin from geodetic measurements. *Journal of Geophysical Research: Solid Earth*,
912 *101*(B12), 27957-27980. doi: 10.1029/96jb02544
- 913 Shen, Z.-K., Sun, J., Zhang, P., Wan, Y., Wang, M., Bürgmann, R., et al. (2009). Slip maxima at
914 fault junctions and rupturing of barriers during the 2008 Wenchuan earthquake. *Nature*
915 *Geoscience*, *2*(10), 718-724. doi: 10.1038/ngeo636
- 916 Shen, Z.-K., Wang, M., Li, Y., Jackson, D. D., Yin, A., Dong, D., & Fang, P. (2001). Crustal
917 deformation along the Altyn Tagh fault system, western China, from GPS. *Journal of*
918 *Geophysical Research: Solid Earth*, *106*(B12), 30607-30621. doi: 10.1029/2001JB000349
- 919 Shen, Z.-K., Wang, M., Zeng, Y., & Wang, F. (2015). Optimal Interpolation of Spatially
920 Discretized Geodetic Data. *Bulletin of the Seismological Society of America*, *105*(4), 2117-2127.
921 doi: 10.1785/0120140247

- 922 Su, X.-N., Meng, G.-J., & Wang, Z. (2016). Methodology and application of GPS strain field
923 estimation based on multi-scaler spherical wavelet. *Chinese J. Geophys. (in Chinese)*, *59*(05),
924 1585-1595. doi: 10.6038/cjg20160504
- 925 Tape, C., Musé, P., Simons, M., Dong, D., & Webb, F. (2009). Multiscale estimation of GPS
926 velocity fields. *Geophysical Journal International*, *179*(2), 945-971. doi: 10.1111/j.1365-
927 246X.2009.04337.x
- 928 Thatcher, W. (2007). Microplate model for the present-day deformation of Tibet. *Journal of*
929 *Geophysical Research*, *112*(B1). doi: 10.1029/2005jb004244
- 930 Walck, M. C., & Clayton, R. W. (1987). P wave velocity variations in the Coso region,
931 California, derived from local earthquake travel times. *Journal of Geophysical Research: Solid*
932 *Earth*, *92*(B1), 393-405. doi: 10.1029/JB092iB01p00393
- 933 Wang, H., Liu, M., Cao, J., Shen, X., & Zhang, G. (2011). Slip rates and seismic moment deficits
934 on major active faults in mainland China. *Journal of Geophysical Research*, *116*(B2), B02405.
935 doi: 10.1029/2010jb007821
- 936 Wang, M., & Shen, Z. K. (2020). Present - Day Crustal Deformation of Continental China
937 Derived From GPS and Its Tectonic Implications. *Journal of Geophysical Research: Solid Earth*,
938 *125*(2), e2019JB018774. doi: 10.1029/2019jb018774
- 939 Wang, Q., Zhang, P.-Z., Freymueller, J. T., Bilham, R., Larson, K. M., Lai, X. a., et al. (2001).
940 Present-Day Crustal Deformation in China Constrained by Global Positioning System
941 Measurements. *Science*, *294*(5542), 574-577. doi: 10.1126/science.106364
- 942 Wang, W., Qiao, X., Yang, S., & Wang, D. (2017). Present-day velocity field and block
943 kinematics of Tibetan Plateau from GPS measurements. *Geophysical Journal International*,
944 *208*(2), 1088-1102. doi: 10.1093/gji/ggw445

- 945 Wang, W., Zhao, B., Qiao, X., & Ding, K. (2022). Block Kinematics in North China From GPS
946 Measurements. *Geochemistry, Geophysics, Geosystems*, 23(3). doi: 10.1029/2021gc010216
- 947 Wang, Y., Deng, Y., Shi, F., & Peng, Z. (2020). The Indo–Eurasia convergent margin and
948 earthquakes in and around Tibetan Plateau. *Journal of Mineralogical and Petrological Sciences*,
949 115(2), 118-137. doi:
- 950 Wang, Z., & Dahlen, F. (1995). Spherical - spline parameterization of three - dimensional Earth
951 models. *Geophysical Research Letters*, 22(22), 3099-3102. doi: 10.1029/95GL03080
- 952 Wang, Z., Tromp, J., & Ekström, G. (1998). Global and regional surface-wave inversions: A
953 spherical-spline parameterization. *Geophysical Research Letters*, 25(2), 207-210. doi:
954 10.1029/97gl03634
- 955 Wei, S., Chen, Y. J., Sandvol, E., Zhou, S., Yue, H., Jin, G., et al. (2010). Regional earthquakes
956 in northern Tibetan Plateau: Implications for lithospheric strength in Tibet. *Geophysical*
957 *Research Letters*, 37(19). doi:
- 958 Wei, W., Dijin, W., Bin, Z., Yong, H., Caihong, Z., Kai, T., & Shaomin, Y. (2014). Horizontal
959 crustal deformation in Chinese Mainland analyzed by CMONOC GPS data from 2009–2013.
960 *Geodesy and Geodynamics*, 5(3), 41-45. doi: 10.3724/SP.J.1246.2014.03041
- 961 Wieczorek, M. A., & Meschede, M. (2018). SHTools: Tools for Working with Spherical
962 Harmonics. *Geochemistry, Geophysics, Geosystems*, 19(8), 2574-2592. doi:
963 10.1029/2018gc007529
- 964 Wiggins, R. A. (1972). The general linear inverse problem: Implication of surface waves and
965 free oscillations for earth structure. *Reviews of Geophysics*, 10(1), 251-285. doi:
966 10.1029/RG010i001p00251

- 967 Wu, Y., Jiang, Z.-S., Yang, G.-h., Fang, Y., & Wang, W.-X. (2009). The Method of GPS Strain
968 Calculation in Whole Mode Using Least Square Collocation on Sphere Surface and Its
969 Application. *Chinese J. Geophys. (in Chinese)*, 52(07), 1707-1714. doi: 10.1002/cjg2.1398
- 970 Wu, Y., Jiang, Z., Yang, G., Wei, W., & Liu, X. (2011). Comparison of GPS strain rate
971 computing methods and their reliability. *Geophysical Journal International*, 185(2), 703-717.
972 doi: 10.1111/j.1365-246X.2011.04976.x
- 973 Xiong, Z., Zhuang, J., Zhou, S., Matsu'ura, M., Hao, M., & Wang, Q. (2021). Crustal strain-rate
974 fields estimated from GNSS data with a Bayesian approach and its correlation to seismic activity
975 in Mainland China. *Tectonophysics*, 815. doi: 10.1016/j.tecto.2021.229003
- 976 Xu, X., X.-Y. Wu, Yu, G., Tan, X., & Li, K. (2017). Seismo-geological signatures for identifying
977 $M \geq 7.0$ earthquake risk areas and their preliminary application in mainland China. *seismology*
978 *and geology*, 39(02), 219-275. doi: 10.3969/j.issn.0253-4967.2017.02
- 979 Yang, Q.-Y., Santosh, M., & Dong, G. (2014). Late Palaeoproterozoic post-collisional
980 magmatism in the North China Craton: geochemistry, zircon U–Pb geochronology, and Hf
981 isotope of the pyroxenite–gabbro–diorite suite from Xinghe, Inner Mongolia. *International*
982 *Geology Review*, 56(8), 959-984. doi: 10.1080/00206814.2014.908421
- 983 Yin, A. (2010). Cenozoic tectonic evolution of Asia: A preliminary synthesis. *Tectonophysics*,
984 488(1-4), 293-325. doi: 10.1016/j.tecto.2009.06.002
- 985 Yin, A., & Harrison, T. M. (2000). Geologic evolution of the Himalayan-Tibetan orogen. *Annual*
986 *Review of Earth and Planetary Sciences*, 28(1), 211-280. doi: 10.1146/annurev.earth.28.1.211
- 987 Yin, A., Yu, X., Shen, Z.-K., & Liu-Zeng, J. (2015). A possible seismic gap and high earthquake
988 hazard in the North China Basin. *Geology*, 43(1), 19-22. doi: 10.1130/g35986.1

- 989 Yu, J., Tan, K., Zhang, C., Zhao, B., Wang, D., & Li, Q. (2019). Present-day crustal movement
990 of the Chinese mainland based on Global Navigation Satellite System data from 1998 to 2018.
991 *Advances in Space Research*, 63(2), 840-856. doi: 10.1016/j.asr.2018.10.001
- 992 Yu, Y., & Chen, Y. J. (2016). Seismic anisotropy beneath the southern Ordos block and the
993 Qinling-Dabie orogen, China: Eastward Tibetan asthenospheric flow around the southern Ordos.
994 *Earth and Planetary Science Letters*, 455, 1-6. doi: 10.1016/j.epsl.2016.08.026
- 995 Zhang, F., Wu, Q., Li, Y., Zhang, R., Sun, L., Pan, J., & Ding, Z. (2018). Seismic Tomography
996 of Eastern Tibet: Implications for the Tibetan Plateau Growth. *Tectonics*, 37(9), 2833-2847. doi:
997 10.1029/2018tc004977
- 998 Zhang, P.-Z. (2013). A review on active tectonics and deep crustal processes of the Western
999 Sichuan region, eastern margin of the Tibetan Plateau. *Tectonophysics*, 584, 7-22. doi:
1000 10.1016/j.tecto.2012.02.021
- 1001 Zhang, P.-Z., Shen, Z., Wang, M., Gan, W., Bürgmann, R., Molnar, P., et al. (2004). Continuous
1002 deformation of the Tibetan Plateau from global positioning system data. *Geology*, 32(9), 809-
1003 812. doi: 10.1130/G20554.1
- 1004 Zhang, Z., Yao, H., & Yang, Y. (2020). Shear wave velocity structure of the crust and upper
1005 mantle in Southeastern Tibet and its geodynamic implications. *Science China Earth Sciences*, 63,
1006 1278-1293. doi:
- 1007 Zhao, D., Qu, C., Shan, X., Gong, W., Zhang, Y., & Zhang, G. (2018). InSAR and GPS derived
1008 coseismic deformation and fault model of the 2017 Ms7. 0 Jiuzhaigou earthquake in the
1009 Northeast Bayanhar block. *Tectonophysics*, 726, 86-99. doi:

- 1010 Zhao, G., Unsworth, M. J., Zhan, Y., Wang, L., Chen, X., Jones, A. G., et al. (2012). Crustal
1011 structure and rheology of the Longmenshan and Wenchuan Mw 7.9 earthquake epicentral area
1012 from magnetotelluric data. *Geology*, *40*(12), 1139-1142. doi:
- 1013 Zhao, J., Yuan, Z., Ren, J., Jiang, Z., Yao, Q., Zhou, Z., et al. (2022). Acceleration of Deep Slip
1014 Along the Longmenshan Fault Plane Before the 2008 M8.0 Wenchuan Earthquake. *Frontiers in*
1015 *Earth Science*, *10*. doi: 10.3389/feart.2022.830317
- 1016 Zheng, G., Wang, H., Wright, T. J., Lou, Y., Zhang, R., Zhang, W., et al. (2017). Crustal
1017 Deformation in the India-Eurasia Collision Zone From 25 Years of GPS Measurements. *Journal*
1018 *of Geophysical Research: Solid Earth*, *122*(11), 9290-9312. doi: 10.1002/2017jb014465
- 1019 Zheng, T., Ding, Z., Ning, J., Chang, L., Wang, X., Kong, F., et al. (2018). Crustal azimuthal
1020 anisotropy beneath the southeastern Tibetan Plateau and its geodynamic implications. *Journal of*
1021 *Geophysical Research: Solid Earth*, *123*(11), 9733-9749. doi:
- 1022 Zheng, Y.-F., Xiao, W.-J., & Zhao, G. (2013). Introduction to tectonics of China. *Gondwana*
1023 *Research*, *23*(4), 1189-1206. doi: 10.1016/j.gr.2012.10.001
- 1024 Zhu, S., Chen, J., & Shi, Y. (2022). Earthquake potential in the peripheral zones of the Ordos
1025 Block based on contemporary GPS strain rates and seismicity. *Tectonophysics*, *824*. doi:
1026 10.1016/j.tecto.2022.229224
- 1027 Zhu, S., & Shi, Y. (2011). Estimation of GPS strain rate and its error analysis in the Chinese
1028 continent. *Journal of Asian Earth Sciences*, *40*(1), 351-362. doi: 10.1016/j.jseaes.2010.06.007
1029